applied sciences

MDPI

Article

Molecular Docking and Pharmacokinetic Profiling of GC-MS-Identified Phytochemicals from *Peganum harmala*-Derived Essential Oil: In Silico Assessment of Binding Affinity Toward PCOS-Related Targets

Waad A. Al-Otaibi [1,*,†] and Sahar M. AlMotwaa [2,†]

[1] Department of Chemistry, College of Science and Humanities, Shaqra University, Shaqra 11961, Saudi Arabia
[2] Applied College, Shaqra University, Shaqra 11961, Saudi Arabia
* Correspondence: w.otaibi@su.edu.sa
† These authors contributed equally to this work.

Abstract

Polycystic Ovary Syndrome (PCOS) is a prevalent endocrine disorder in women of reproductive age, characterized by hyperandrogenism, insulin resistance, and ovarian dysfunction. Current therapies are often associated with adverse effects, highlighting the need for safer therapeutic alternatives. *Peganum harmala* (*P. harmala*), a medicinal plant rich in bioactive metabolites, was investigated through in silico approaches to identify compounds with predicted binding affinity for the androgen receptor (AR), steroid 17α-hydroxylase/17,20-lyase (CYP17A1), and glycogen synthase kinase-3 beta (GSK-3β). GC-MS analysis of *P. harmala* leaf essential oil collected in Riyadh, Saudi Arabia, identified 109 compounds, with terpenoids as the dominant class (21.89%). The major constituents were cis-chrysanthenyl acetate (3.48%), cis-β-damascenone (3.06%), farnesylacetone (1.44%), β-calacorene (1.36%), dihydroedulan II (1.04%), and trans-calamenene (0.46%). In silico ADMET evaluation indicated that most compounds complied with Lipinski's rule of five and showed favorable predicted pharmacokinetic properties. Safety profiling suggested an overall acceptable toxicity profile, with minimal predicted CYP450 inhibition, except for L11, which showed broader inhibitory potential. Molecular docking showed that L15 (trans-calamenene), L14 (dihydroedulan II), L6 (β-calacorene), L3 (farnesylacetone), and L8 exhibited higher predicted binding affinity toward the androgen receptor; L3, L10 (cis-β-damascenone), and L16 (cis-chrysanthenyl acetate) interacted with CYP17A1, while L3, L9, and L6 exhibited higher affinity toward GSK-3β. Overall, these findings provide hypothesis-generating in silico predictions of ligand–target binding affinities and drug-likeness profiles. These computational findings highlight the importance of future experimental investigations to substantiate the biological activity, pharmacokinetic behavior, and safety profile of *P. harmala* constituents.

Keywords: polycystic ovary syndrome; *Peganum harmala*; androgen receptor (AR); steroid 17α-hydroxylase/17,20 lyase (CYP17A1); glycogen synthase kinase 3 beta (GSK-3β); terpenoids; GC-MS; molecular docking; ADMET

Check for updates

Academic Editor: Alessandro Arcovito

Received: 10 March 2026
Revised: 21 April 2026
Accepted: 22 April 2026
Published: 25 April 2026

Copyright: © 2026 by the authors. Licensee MDPI, Basel, Switzerland. This article is an open access article distributed under the terms and conditions of the Creative Commons Attribution (CC BY) license.

1. Introduction

Polycystic Ovary Syndrome (PCOS) is a multifaceted endocrine disorder that affects 4–20% of women of reproductive age [1]. It is characterized by hyperandrogenism, insulin

resistance, menstrual irregularities, and infertility [2]. The pathogenesis of PCOS is closely associated with systemic low-grade chronic inflammation (SLCI), which plays a pivotal role in disease progression [3]. Hyperactivation of related signaling pathways contributes to androgen overproduction, insulin resistance, and ovarian dysfunction [1]. The molecular targets, i.e., androgen receptor (AR), steroid 17α-hydroxylase/17,20 lyase (CYP17A1), and glycogen synthase kinase-3 beta (GSK-3β), have been identified as central mediators of the hormonal and metabolic disturbances in PCOS, thereby presenting promising avenues for therapeutic intervention [4–6]. However, the current pharmacological treatment strategies for PCOS, such as use of oral contraceptives, insulin sensitizers, ovulation induction agents and anti-androgens, primarily provide symptomatic relief which are often accompanied by adverse effects, thereby highlighting the need for safer and more effective alternatives [7].

In Saudi Arabia, it has been reported that 88.4% of adults (predominantly females) use herbal medicines, with 84.3% of the users interested in traditional remedies, while 88.7% use them for therapeutic purposes [8]. Among the medicinal plants used, *Peganum harmala* (*P. harmala*) is particularly significant. The genus *Peganum* comprises perennial, herbaceous flowering plants ranging from glabrous to pubescent, with short creeping roots [9]. This perennial species of the *Zygophyllaceae* family is rich in alkaloids, flavonoids, and terpenoids with anti-inflammatory, antidiabetic antioxidants, antimicrobial, analgesic, and endocrine-modulating properties [10–14]. In addition, it has been employed in the management of various conditions such as dermatological and gastrointestinal disorders, chronic rheumatism, and tumors [10].

The potential therapeutic effects of *P. harmala*, from either its essential oil or other plant components, have not been previously reported in the treatment of women's health issues, gynecological disorders, or inflammatory conditions. Although it has traditionally been used as a tonic to regulate the menstrual cycle, alleviate menstrual discomfort, enhance fertility, and address various women's health issues [15]. Scientific evidence supporting the use of this plant for treating conditions such as Polycystic Ovary Syndrome (PCOS) or for its anti-inflammatory effects remains limited. Research on the chemical composition of *P. harmala* essential oils remains limited. Most existing studies have analyzed oils from whole aerial parts or seeds, without specifically evaluating leaf constituents. This highlights a critical research gap regarding their potential role in PCOS [16–18]. The predominant constituents reported comprise oxygenated monoterpenes, sesquiterpenes, eugenol, and oxygenated sesquiterpenes, with notable variations between regions [16,17]. Environmental and geographic conditions exert significant impacts on plant growth and the synthesis of secondary metabolites, thereby affecting their safety, effectiveness, and biological properties. This highlights the importance of accounting for local environmental factors in pharmacological research [19]. In previous studies, terpenoids have been shown to be bioactive compounds with potential relevance in PCOS. Some evidence suggests that their anti-inflammatory and antioxidant properties could help modulate inflammatory responses, which may be relevant to hormonal and metabolic dysregulation associated with PCOS pathophysiology [20].

However, there is a lack of studies evaluating *P. harmala* leaf constituents through molecular docking against key targets associated with polycystic ovary syndrome (AR, CYP17A1, GSK-3β), representing a significant research gap, despite the potential of structure-based computational approaches to systematically identify promising compounds. This approach enables the preliminary identification of compounds that may be associated with hormonal regulation and disease-related metabolic pathways, based on computational predictions. Accordingly, the present study aimed to explore the in silico binding potential of *P. harmala* compounds with these key targets, providing initial insights into their possible

mechanisms of action and laying the groundwork for future experimental validation and the development of plant-derived candidates for therapeutic research in PCOS.

2. Materials and Chemicals

All reagents employed in this study were of ACS grade and were sourced from Sigma-Aldrich (St. Louis, MO, USA), unless otherwise stated. Laboratory glassware such as sealed vials, Pyrex® glassware (funnels, pipettes, conical flasks, measuring cylinders), filter papers, and flexible weighing boats were procured from Al-Rowad for Medical Equipment Supply (Jeddah, Saudi Arabia). Electronic micropipettes of various sizes, Clevenger apparatus, and high-precision electronic balance were obtained from ALSAGGAF Medical Service Est. (Jeddah, Saudi Arabia), while water filtration system was supplied by Al-Zamil Industry, Trade and Transport (Riyadh, Saudi Arabia).

2.1. Methods

2.1.1. Plant Material Collection and Preparation

P. harmala leaves were collected from naturally growing plants in Riyadh province (Latitude 25°19′00.8″ N; Longitude 46°09′39.9″ E) and kept in polyethylene bags. The collected samples were shade-dried individually for 10 days at room temperature (25 ± 2 °C).

2.1.2. Extraction and Analysis of Essential Oils

The essential oils were hydro-distilled from 200 g of separated, shade-dried leaves in 1100 mL of distilled water at 60 °C for 9 h, using a Clevenger-type apparatus.

2.1.3. Recovery of Essential Oils and Calculation of Yield

The aqueous fraction of the mixture consisting of essential oil and leaf-derived water was filtered into a separatory funnel. Then, the essential oil was isolated by adding 5 mL of n-hexane to the separating funnel. The liquid–liquid extraction process was repeated twice to ensure complete removal of oil from the aqueous phase. Then, the n-hexane solvent was evaporated from the oil extract using a rotary evaporator, and residual moisture was eliminated using anhydrous sodium sulfate. The essential oil obtained was preserved at 4 °C in a sealed, dark container prior to analysis. The yield (Y) of essential oil was calculated using the following formula:

$$Y\ (\%) = \frac{Wo}{Mp} \times 100$$

Wo is the weight of essential oil collected, and *Mp* is mass of plant material used in the extraction process.

2.2. Gas Chromatography-Mass Spectrometry (GC-MS) Analysis

Analysis of the essential oil from *P. harmala* leaves was performed using a Hewlett-Packard GC-MS system coupled with a 7000D triple quadrupole detector (Agilent Technologies, Palo Alto, CA, USA). Separation was achieved on an HP-5MS column (30 m × 0.25 mm × 0.25 µm film thickness) using helium as the carrier gas at a flow rate of 0.5 mL/min. The analysis was conducted in split mode (1:25) with an injection volume of 0.2 µL (1:10 n-hexane v/v). The injector temperature was set at 250 °C, and the oven temperature was programmed from 60 °C (8 min) to 280 °C at 2 °C/min, followed by holding at 280 °C for 15 min. Electron impact ionization was performed at 70 eV over a mass range of 30–550 m/z. Compounds were identified using AMDIS (Automated Mass Spectral Deconvolution and Identification System), version 2.73 (National Institute of Standards and Technology, Gaithersburg, MD, USA) and by comparison of mass spectra with the Wiley

and NIST libraries. Retention indices (RI) were calculated relative to n-alkanes (C8–C22) and used in combination with retention times and mass spectral matching for compound identification. Relative abundances were determined based on peak areas.

2.2.1. Chemical Classification of Essential Oil Compounds from *P. harmala* Leaves

The compounds were classified according to their chemical structures using the PubChem Database [21], with additional reference to the KEGG Phytochemical Compounds guide or the Medical Subject Headings (MeSH) tree classification, when required. Each compound was assigned a PubChem Compound Accession Identifier (CID) and arranged according to its elution time in the GC-MS profile of the sample.

2.2.2. Compound Selection for Molecular Docking

Among the 109 compounds identified by GC-MS analysis, 17 major constituents with relative abundances greater than 1% were selected as ligands for molecular docking in subsequent computational studies. This selection was intended to prioritize the most representative components of the oil's chemical profile, while low-abundance compounds were excluded to focus on the dominant bioactive constituents. The selected compounds were subjected to in silico analyses, including Lipinski-based drug-likeness, ADMET profiling, and safety assessment. In addition, preliminary screening of drug-likeness and bioavailability was performed to identify compounds with the highest relevance and potential relevance to PCOS-related molecular targets.

2.3. In Silico Analyses of the Compounds

2.3.1. Preparation of the Selected Ligands and Target Proteins

The ligands were downloaded from PubChem https://pubchem.ncbi.nlm.nih.gov/ (accessed on 20 January 2025) in (2D) *sdf format to evaluate their potential interactions with the target proteins [22]. They subsequently converted into three-dimensional (3D) structures in PDB format using the Online SMILES Translator https://cactus.nci.nih.gov/translate (accessed on 5 February 2025) to enable virtual screening.

2.3.2. Preparation of Target Receptors and Identification of Active Sites

The crystal structures of the androgen receptor (AR), steroid 17α-hydroxylase/17,20 lyase (CYP17A1), and glycogen synthase kinase-3 beta (GSK-3β) were retrieved in PDB format from the RCSB Protein Data Bank https://www.rcsb.org (accessed on 13 June 2025) [23]. These proteins were selcted as therapeutic targets for polycystic ovary syndrome (PCOS) due to their roles in androgen signaling, steroid biosynthesis, and metabolic regulation [4–6]. Protein preparation was performed using Biovia Discovery Studio (2019), where co-crystallized ligands, water molecules, and heteroatoms were removed, and hydrogen atoms were added to stabilize protein structures [24]. Active binding sites were identified to guide docking simulations, and binding pockets and key residues were further analyzed using Biovia Discovery Studio [24]. This approach facilitates accurate prediction of ligand–protein interactions and improves docking reliability [25].

2.3.3. Molecular Docking (MD) and Visualization

Docking was performed using PyRx software, version 0.8 incorporating AutoDock 4 (The Scripps Research Institute, La Jolla, CA, USA). Protein structures were converted to PDBQT format using the "make macromolecule" option, while ligands were energy-minimized using the Universal Force Field (UFF) prior to docking [26,27]. Docking was performed at experimentally determined active sites corresponding to each protein, i.e., androgen receptor (PDB: 2AM9): PHE 891, LEU 701, ASN 705, LEU 880, THR 877, MET 895, MET 742, ILE 899, LEU 704, TRP 741, GLY 708, LEU 707, MET 745, ARG 752, MET 749,

GLN 711, PHE 764, MET 787, VAL 746, LEU 873, MET 780, and PHE 876; CYP17A1 (PDB: 6WW0): ASN 202, TYR 201, ILE 205, ILE 206, GLU 305, LEU 209, PHE 114, VAL 482, VAL 483, ILE 371, ALA 367, VAL 366, ARG 239, ALA 105, GLY 301, GLY 297, ASP 298, ALA 113, ALA 302, and THR 306; GSK-3β (PDB: 1PYX): ILE 62, GLY 63, ASN 64, GLY 65, SER 66, PHE 67, GLY 68, VAL 70, ALA 83, LYS 85, VAL 110, LEU 132, ASP 133, TYR 134, VAL 135, THR 138, ASP 181, LYS 183, GLN 185, ASN 186, LEU 188, and ASP 200.

All docking calculations were performed assuming a rigid receptor model, while ligand flexibility was retained. Polar hydrogen atoms were added, and appropriate protonation states were assigned to both ligands and protein residues at physiological pH conditionsThe docking grid was centered on the co-crystallized ligand to cover all key active-site residues (Table 1). Docking parameters were set as follows: exhaustiveness = 8, and the number of binding poses generated per ligand was set to 9. The best binding conformation was selected based on the lowest binding free energy and interaction profile. Protocol validatation was performed through redocking of the co-crystallized ligand for each target protein, and the root-mean-square deviation (RMSD) between docked and experimental poses was calculated. RMSD values below 3 Å were considered indicative of acceptable docking accuracy. Docking results were visualized using Biovia Discovery Studio 2019 [24]. Binding affinities were calculated using AutoDock Vina (kcal/mol), and the lowest-energy complex was selected for detailed interaction analysis, including bond types, distances, and key amino acid residues.

Table 1. Grid box parameters (center and size) of the redocking process of selected proteins.

PDB	Ligand ID	Grid Box (x, y, z)		Binding Affinity (Kcal mol^{-1}) (RMSD in Å)	Types of Interactions in Redocking Processes
		Center	*Size*		
2AM9	TES $C_{19}H_{28}O_2$	27.4457803953 −0.1816644422 1.27187634324	25.0 25.0 24.99342837	−11 1.95 (Å)	Conventional Hydrogen Bonds: SC D-H: -NH GLN 711 To O=C (2.58 Å) SC D-H: -NH ARG 752 To HO- (2.38 Å) SC A-H: -O- THR 877 To HO- (2.20 Å) Hydrophobic interactions: Alkyl: MET 745 (3.99 Å)
6WW0	UDJ $C_{24}H_{31}NO$	−26.0641 43.0676975203 −54.458354514	25.0 33.1167950406 42.9233231978	−10.9 1.65 (Å)	Conventional Hydrogen bonds: SC D-H: NH- ASN 202 to O=C (2.06 Å) Carbon-Hydrogen bond: SC D-H: H-C- ASN 202 To O=C (3.53 Å) Hydrophobic interactions: Alkyl: ALA 113, ALA 302, VAL 482 (3.97, 3.66, 4.27 Å)
1PYX	AMP-PNP $C_{10}H_{17}N_6O_{12}P_3$	36.7986521404 7.48239284074 36.2857200105	21.072714888 17.4513804538 23.4076612238	−7.6 1.95 (Å)	Conventional Hydrogen bonds: BB A-H: O=C ASN 64 to HO- (2.62, 2.25 Å) BB A-H: O=C VAL135 to HN- (2.42 Å) SC D-H: HN- ASN 64 to O=P (2.16 Å) SC D-H: HN- LYS 183 to O=C (2.97 Å) SC D-H: HN- GLN 185 to O=C (2.34 Å) Carbon-Hydrogen bond: SC D-H: HC- GLY 63 to O-P (3.80 Å) Electrostatic and Others: Unfavorable donor-donor: BB D-H: HN- ASN 64 To HO- (2.39. 3.30 Å)

2AM9: Human androgen receptor; **6WW0**: Cytochrome P450 17A1 (CYP17A1); **1PYX**: Glycogen synthase kinase-3 beta; **Tes**: Testosterone; **UDJ**: 3-keto-5alpha-238 abiraterone; **BB**: Backbone; **SC**: Side chain; **D-H**: Hydrogen donor; 239 **A-H**: Hydrogen acceptor.

2.3.4. ADMET Profiling of the Identified Compounds

Assessing the ADMET profile of new compounds at an early stage is crucial. It refers to Absorption, Distribution, Metabolism, Excretion/Elimination, and Toxicity [28]. A drug or drug-like compound must have attributes beyond high bioactivity and low toxicity, to be a promising candidate. A good pharmacokinetic profile is an exclusively important parameter that should be assessed for any novel compound in drug/drug-like compound discovery. To achieve this, an online SMILES translator http://cactus.nci.nih.gov/translate/ (accessed on 27 June 2025) was used to interpret the bioactive compounds (*sdf) format obtained previously in preparation step in SMILE format. The ADME properties of the compounds were assessed using SwissADME, a web-based tool http://www.swissadme.ch (accessed on 14 July 2025), to predict key pharmacokinetic parameters including absorption, distribution, metabolism, and excretion [29].

2.3.5. Prediction of Physicochemical Properties of Identified Compounds

The physicochemical attributes predicted were molecular mass, octanol–water partition coefficient, Log P (which refers to high lipophilicity), the number of rotating atomic bonds, Activity of the Polar Surface (PSA), and H-bond donors/acceptors. These characteristics were assessed to evaluate the compounds' oral bioavailability based on Lipinski's rule of five (Ro5) [30], a widely used rule-based filter for assessing drug-likeness and predicting oral absorption. The standard parameters for the rule are molecular mass of compound is acceptable when equal or below 500; acceptable range of $\leq$5 for a H-bond donor; acceptable range of $\leq$10 for hydrogen bond acceptor; ideal range of $\leq$5 for elevated lipophilicity which is measured in LogP, and permissible range of 40 to 130 for molar refractivity. Therefore, it is unlikely that a compound will be orally accessible as a medication if its characteristics fall outside of these ranges [31].

2.3.6. Toxicity Prediction

The toxicity profiles of the selected compounds were predicted using the ProTox-II webserver https://tox.charite.de/protox3/ (accessed on 26 July 2025), an in silico tool that estimates various toxicity endpoints including LD_{50}, toxicity class, hepatotoxicity, carcinogenicity, immunotoxicity, mutagenicity, and cytotoxicity [32]. Predicted values for total clearance, renal OCT2 substrate, AMES toxicity, and skin sensitization were obtained using the pkCSM webserver https://biosig.lab.uq.edu.au/pkcsm/prediction (accessed on 28 July 2025), which provides predictive models for these excretion and toxicity endpoints as part of its ADMET profiling. The SMILES format of each compound was used as input for the prediction [33].

3. Results and Discussion

3.1. Chemical Composition and Major Constituents of Harmala Plant Leaf Essential Oil Revealed by GC-MS Analysis

The extraction of 200 g of *P. harmala* leaves yielded 0.025% of essential oil. Although this yield is relatively low, it does not undermine the pharmacological significance of the plant, as essential oils can contain highly potent bioactive constituents even at minimal concentrations. Accordingly, the present study focuses on the identification of these compounds as potential lead structures rather than their immediate applicability for large-scale production.

Notably, *P. harmala* is a widely distributed desert plant, representing a renewable and cost-effective natural resource [34]. Its natural abundance and ability to thrive under harsh environmental conditions reduce the need for intensive cultivation and partially compensate for the low extraction yield. Furthermore, advancements in extraction techniques, as

well as synthetic and semi-synthetic approaches, may enhance the overall feasibility and accessibility of these bioactive compounds in future applications.

Using the NIST database, the metabolites in the samples were identified through GC-MS (Figure 1). Compounds with a similarity score higher than 80 were selected. The detected metabolites, representing a diverse range of major chemical classes along with their corresponding values, are presented in Table S1. As presented in Figure 2A,B, terpenoids were the most prominent, accounting for approximately 21.89% of the total composition. Within this class, the notable compounds were chrysanthenyl acetate (3.48%), cis-β-damascenone (3.06%), cadalene (2.65%), and (Z)-beta-ionone (1.99%). The other components were squalene (1.65%), farnesylacetone (1.44%), beta-calacorene (1.36%), dihydroedulan II (1.04%), alpha-corocalene (0.89%), 4-(2,6,6-trimethylcyclohexa-1,3-dienyl)but-3-en-2-one (0.80%), phytol (0.65%), 4,8,12-tetradecatrienal, 5,9,13-trimethyl-(0.55%), and trans-calamenene (0.46%).

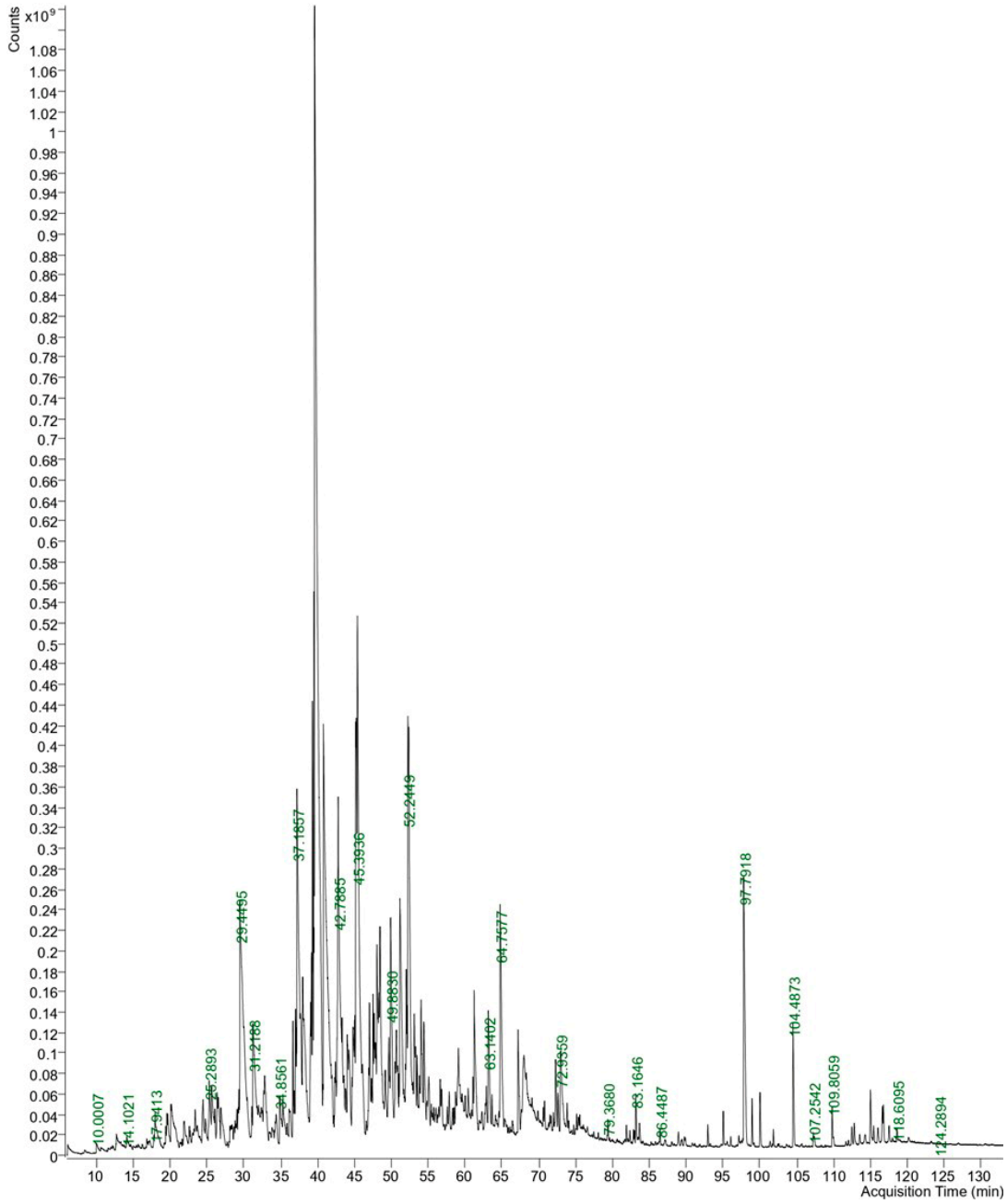


Figure 1. Chromatogram of essential oil of *P. harmala* leaves.

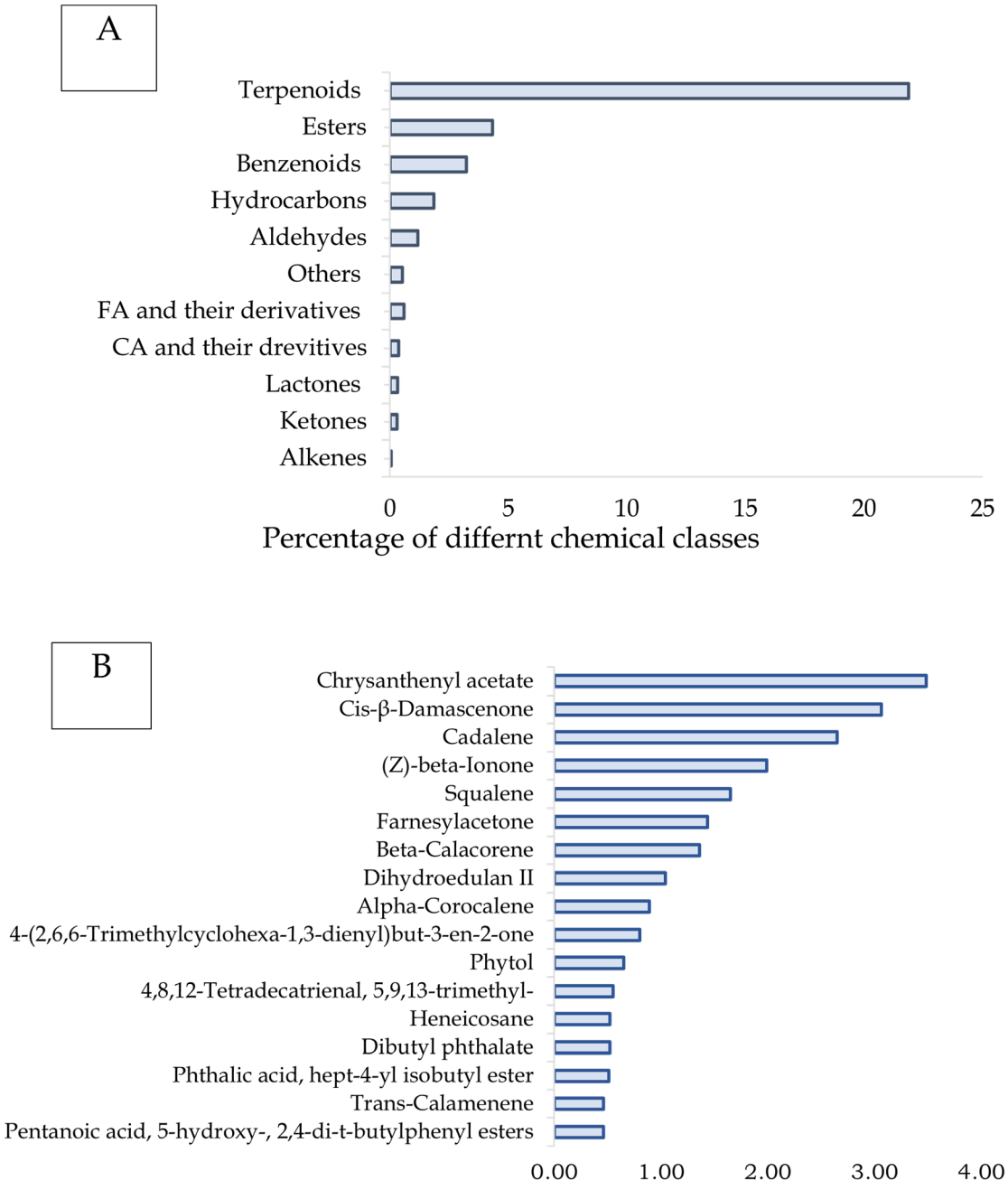


Figure 2. (**A**) Major phytochemical constituents of *P. harmala* identified via GC-MS analysis. (**B**) Relative abundance of minor phytochemical constituents of *P. harmala* detected using GC-MS analysis.

Pentanoic acid and 5-hydroxy-, 2,4-di-t-butylphenyl ester accounted for about 97% of the total ester compounds. Benzenoids consisting mainly of dibutyl phthalate and phthalic acid, hept-4-yl isobutyl ester, represent about 32% of the total benzenoid compounds. Hydrocarbons accounted for 1.85%, with heneicosane (0.52%) being the most predominant compound. Safranal and beta-homocyclocitral were the main aldehydes which accounted for 0.40 and 0.38% of the total identified compounds, respectively. To date, only a limited number of researchers have carried out studies on the chemical compositions of essential oils derived from the leaves of *P. harmala*. The essential oil yield from dried *P. harmala* leaves varied across regions in southern Algeria, with 0.217% in Bougtob and 0.211% in Mechria. In the Bougtob sample, 55 compounds were identified, with carvone (21.15%), phytol (17.41%), carbamic acid (3.52%), lauric acid (2.10%), and thymol (1.77%) being the main constituents. In contrast, the Mechria sample contained 47 compounds dominated by

phytol (10.24%), carvone (5.92%), tetrapentacontane (2.80%), phytone (2.18%), butylated hydroxytoluene (1.48%), and lauric acid (1.39%) [35].

Earlier studies in Morocco found that the dry leaves contained nineteen identified volatile components comprising mainly 2,3-dihydrobenzofurane (12.5%) and propylic acid (11.1%) [36]. These variations may be due to differences in plant parts investigated, extraction process, environmental factors, growth season, and genetics [37]. On the other hand, previous investigations concentrated mainly on the profiles of *P. harmala* oils from seeds or fruits gathered from various areas such as Morocco, Algeria, Tunisia, Libya, Egypt, and Iran. Notably, the primary constituents of oils from these countries (except Iran) were mono- and sesquiterpenoids [9]. However, the exact chemical compositions and the types of constituents vary significantly among these studies, thereby reflecting regional differences and methodological variations.

3.2. Data on Drug-Likeness of Ligands via In Silico Analysis

A preliminary in silico drug-likeness evaluation of 17 ligands was performed using SwissADME, and the results are summarized in Table 2. Drug-likeness was assessed based on Ro5, which considers hydrogen bond acceptors ≤ 10, H-bond donors ≤ 5, molecular weight ≤ 500, and MLOGP ≤ 4.15. A compound is generally considered drug-like if it shows no more than one violation of Ro5 [35].

Table 2. In silico drug-likeness of chosen compounds (L1–L17) calculated using the SwissADME web tool.

	MW (g/mol)	#HA	#HD	MLOGP	ESOL Class	Lipinski #Violations	TPSA (Å^2)	#RB	Veber #Violations	MR	Synthetic Accessibility
Rule	**≤500**	**N or O ≤10**	**NH or OH ≤ 5**	**≤4.15**	**P: Poor MS: Moderate Soluble S: Soluble**	**≤1 (NO)**	**≤140**	**≤10**	**≤1 (NO)**	**40 ≤ MR ≤130**	**Easy (0) Very Difficult (10)**
L1	198.3	0	0	5.62	MS	1	0.00	1	0	68.46	1.05
L2	296.57	0	0	7.6	PS	1	0.00	18	1	103.06	2.84
L3	262.43	1	0	4.5	MS	1	17.07	9	0	87.42	3.47
L4	278.34	4	0	3.43	S	0	52.6	10	0	77.84	2.41
L5	296.53	1	1	5.25	MS	1	20.23	13	1	98.94	4.3
L6	200.32	0	0	5.36	MS	1	0.00	1	0	68.39	2.64
L7	200.32	0	0	5.36	MS	1	0.00	1	0	68.55	2.81
L8	194.31	1	0	2.85	S	0	17.07	3	0	61.96	3.85
L9	248.40	1	0	2.85	S	0	17.07	9	0	82.61	3.85
L10	190.28	1	0	2.85	S	0	17.07	2	0	61.01	3.64
L11	306.45	3	1	4.35	MS	0	46.53	8	0	92.09	3.64
L12	192.30	1	0	2.94	S	0	17.07	2	0	61.48	3.38
L13	410.72	0	0	2.94	S	0	0.00	15	1	143.48	3.38
L14	194.31	1	0	3.15	S	0	9.23	0	0	60.77	4.16
L15	202.34	0	0	5.45	MS	1	0.00	1	0	68.07	2.61
L16	194.27	2	0	2.65	S	0	26.3	2	0	56.12	4.52
L17	320.42	4	0	4.14	MS	0	52.6	11	1	92.26	2.77

MW: molecular weight; #HA: Number of H-atom Acceptor and #HD: Number of H-atom Donor; MR: Molar Reactivity; TPSA: Topological polar surface area (Å^2); #RB: Number of Rotatable Bonds.

All the ligands exhibited acceptable molecular weights ranging from 190.28 to 410.72 g/mol. It is significant to note that ligands L1, L2, L3, L5, L6, L7, and L15 each violated one of Ro5, whereas the remaining ligands complied with all criteria (MLOGP < 4.15). This non-compliance is linked to lipophilicity. L2 exhibited the highest MLOGP, indicating high lipophilicity, which may enhance membrane permeability but could reduce solubility and oral bioavailability [38]. Drug absorption across the lipid bilayer of the membrane is influenced by lipophilicity [39]. The optimal lipophilicity scores used in drug design range from 0 to 5 [40]. In this study, L2 showed the most notable deviation, while L1, L5, L6, L7, and L15 exhibited moderate increases in MLOGP, indicating gradual impacts on membrane permeability and solubility. In contrast, L3 had a slightly elevated lipophilicity and one rule violation, while the remaining ligands exhibited lower lipophilicity scores (MLOGP < 4.15) and complied with the guidelines concerning the number of unacceptable properties.

Approximately 50% of the compounds exhibited favorable solubility, while the rest showed moderate levels, suggesting generally acceptable oral absorption profiles [29]. In contrast, L2 exhibited high lipophilicity, which may reduce its systemic blood levels due to poor absorption and limited bioavailability. In addition, the absence of hydrogen bond donors or acceptors in L1, L2, L6, L7, L13, and L15 further supports their lipophilic character [41]. However, L3, L8, L9, L10, L12 and L14 formed one H-bond acceptor each, which may slightly reduce polarity and influence aqueous solubility. The TPSA values for L3, L8, L9, L10, and L12 were comparable, indicating mild polarity, whereas L14 showed a lower value, reflecting reduced polar surface contribution. L4 and L17 each contained four hydrogen bond acceptors without donors, which may enhance binding interactions with biological targets compared to L16, which contained only two acceptors. The hydrogen bond acceptor-to-donor ratios were 3:1 in L11 and 1:1 in L5, indicating simpler interaction patterns but potentially lower binding flexibility compared with L4, L11, L16, and L17, which showed more balanced hydrogen bonding profiles. L4 and L17 exhibited identical TPSA values (52.6 $Å^2$), while L11 showed a slightly lower value, suggesting moderate polarity that may support biological compatibility. Conversely, L16 and L5 had lower TPSA values, indicating higher membrane permeability but potentially reduced aqueous solubility relative to more polar ligands. All ligands complied with the acceptable rotatable bond threshold (RB $\leq$ 10), indicating adequate molecular flexibility [42]. However, L2, L13, L5 and L17 showed higher rotatable bond counts (18, 15, 13 and 11, respectively), indicating increased flexibility that may exceed the optimal Veber rule threshold (RB $\geq$ 10) and potentially affect binding stability.

All MR values remained within acceptable limits, with L13 showing the highest steric bulk followed by L2, while other ligands displayed lower steric profiles [43]. Among all ligands, L3, L6, L14, and L15 consistently exhibited the most balanced profile across physicochemical parameters and emerged as the most promising candidates for further biological evaluation. In contrast, L2 is the only compound exhibiting dual compliance limitations (MLOGP and RB), which may reduce its overall suitability compared to the rest of the dataset. These factors may negatively affect solubility, permeability, and drug-likeness, while increased lipophilicity and molecular flexibility may further compromise stable interactions with biological targets.

3.3. Pharmacokinetic Properties of the Ligands

The pharmacokinetic and medicinal properties of the selected ligands were evaluated using SwissADME and pkCSM tools [44], as summarized in Table 3. All ligands exhibited negative LogKp values, indicating poor skin permeability and limited suitability for transdermal administration [45]. L2 exhibited the least negative LogKp, attributed to its high lipophilicity, reflecting increased affinity for lipids and non-polar solvents, which may

influence transmembrane transport and ADMET behavior [39]. Only L5 was predicted as a P-gp substrate, suggesting reduced bioavailability due to efflux mechanism [46], whereas the remaining ligands were not affected. Data on blood–brain barrier (BBB) permeability and gastrointestinal absorption (GIA) were predicted using the BOILED-Egg model (SwissADME) (Figure 3). The evaluated ligands exhibited mixed GIA profiles, categorized into low and high absorption. L1, L2, L5, L6, L7, L11, and L15 showed low absorption, indicating potential gastrointestinal limitations related to suboptimal solubility, lipophilicity, and/or permeability, whereas L3, L4, L8, L9, L10, L12, L13, L14, L16, and L17 demonstrated high absorption, reflecting more favorable pharmacokinetic profiles [47]. Predictions of distribution are based on blood–brain barrier (BBB) permeability, which regulates the transfer of drugs from the bloodstream into brain tissue [48]. Ligands L1, L2, L3, L5, L6, L7, L11, and L15 were unable to cross the BBB, which may limit their use in central nervous system (CNS) disorders. In contrast, L4, L8, L9, L10, L12, L13, L14, L16, and L17 showed BBB penetration, indicating potential suitability for neurological applications [38]. However, since the computational approach does not quantify the degree of permeation, the extent may not be substantial enough to cause significant toxic effects on the CNS. Molecular docking studies of ligands with CYP isoforms were performed to evaluate the metabolic interaction profiles of the tested ligands [29]. Inhibition of CYP2C19 was observed only with L4 and L11. As this isoform metabolizes proton pump inhibitors and several antidepressants, its inhibition may enhance drug exposure and associated adverse effects [49]. CYP2C9 inhibition occurred in L3, L5, and L15, potentially prolonging drug activity and increasing bleeding risk via impaired metabolism of NSAIDs and warfarin [50]. Ligands L1, L6, L7, and L15 suppressed CYP2D6 activity, which may elevate plasma drug levels such as antidepressants, antipsychotics, β-blockers and increase toxicity risk [51].

Table 3. Predicted values of pharmacokinetic (ADME) properties for the chosen compounds (L1–L17) calculated using SwissADME.

	Absorption		**Distribution**		**Metabolism Inhibitor**				
	Skin Permeability	**GIA**	**P-gp Substrate**	**BBB Permeability**	**2C19**	**2C9**	**2D6**	**3A4**	**1A2**
	LogKp (cm/s)	**Categorical (High/Low)**	**Categorical (Yes/No)**	**Categorical (Yes/No)**	**Categorical (Yes/No)**				
L1	−3.55	Low	No	No	No	No	Yes	No	No
L2	−0.31	Low	No	No	No	No	No	No	Yes
L3	−3.95	High	No	No	No	Yes	No	No	Yes
L4	−4.8	High	No	Yes	Yes	No	No	No	Yes
L5	−2.29	Low	Yes	No	No	Yes	No	No	No
L6	−4.22	Low	No	No	No	No	Yes	No	No
L7	−4.39	Low	No	No	No	No	Yes	No	No
L8	−5.6	High	No	Yes	No	No	No	No	No
L9	−5.6	High	No	Yes	No	No	No	No	No
L10	−5.2	High	No	Yes	No	No	No	No	Yes
L11	−2.62	Low	No	No	Yes	Yes	No	No	Yes
L12	−5.41	High	No	Yes	No	No	No	No	No
L13	−5.41	High	No	Yes	No	No	No	No	No
L14	−5.1	High	No	Yes	No	No	No	No	No
L15	−3.9	Low	No	No	No	No	Yes	No	No
L16	−5.88	High	No	Yes	No	No	No	No	No
L17	−4.46	Low	No	Yes	No	No	No	No	Yes

GIA: gastrointestinal absorption; LogKp: skin permeation value; P-gp: p P-glycoprotein. Data of BBB and GIA based on BOILED-Egg model.

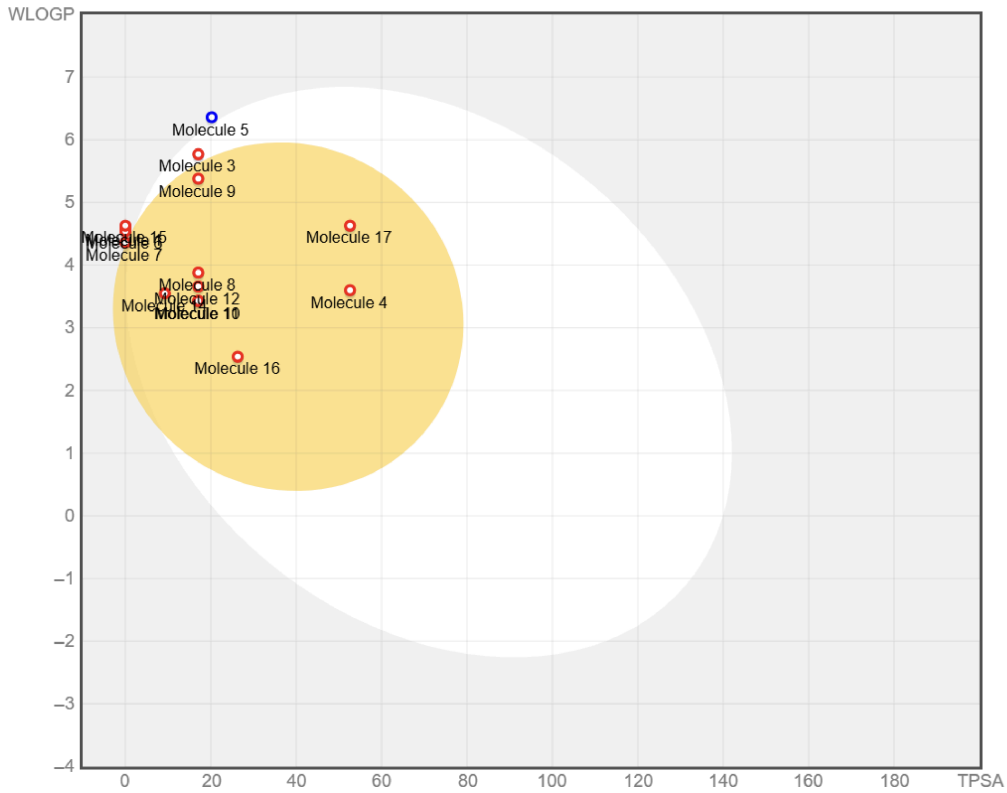


Figure 3. BOILED-Egg model depicting pharmacokinetic properties of the examined compounds. Prediction of passive GIA (white region) and blood–brain barrier penetration (yellow region), based on molecular polarity and lipophilicity. The analyzed compounds were: (1) cadalene, (2) henicosane, (3) farnesylacetone, (4) dibutyl phthalate, (5) phytol, (6) β-calacorene, (7) α-corocalene, (8) 4-(2,6,6-trimethylcyclohexa-1,3-dienyl)but-3-en-2-one, (9) 4,8,12-tetradecatrienal, 5,9,13-trimethyl-, (10) cis-β-damascenone, (11) pentanoic acid, 5-hydroxy-, 2,4-di-t-butylphenyl ester, (12) β-ionone, (13) squalene, (14) dihydroedulan ii, (15) trans-calamenene, (16) cis-chrysanthenyl acetate, and (17) phthalic acid, hept-3-yl isobutyl ester.

However, L8, L12, L14, and L16 had no inhibitory effects on CYP isoforms, suggesting a predictable metabolic profile and lower interaction potential [52]. Notably, L11 displayed multi-CYP inhibition, highlighting potential drug–drug interaction risk. CYP3A4, the most abundant isoform, metabolizes 30–50% of clinically used drugs, including statins, calcium channel blockers, immunosuppressants, and steroids; its inhibition may increase drug exposure and toxicity risk [53]. Similarly, CYP1A2 metabolizes caffeine, theophylline, and certain antipsychotics; its inhibition may elevate plasma levels, particularly for drugs with narrow therapeutic indices [54]. Overall, most ligands showed minimal CYP inhibition, whereas L11 exhibited broad-spectrum inhibitory activity.

As shown in Table 4, the ligands exhibited total clearance rates ranging from 0.13 to 2.03 log mL/min/kg, with L2 having the highest clearance rate. This suggests that the bioavailability of the other ligands is higher than that of L2. None of the ligands was identified as a renal OCT2 substrate, which implies that they might not be actively transported by the OCT2 transporter in the kidneys. This points to the existence of an alternative mechanism for their renal clearance or metabolism.

The toxicity values of the selected compounds were predicted using ProTox II and AMES. The selected compounds were expected not to be hepatotoxic and cytotoxic. The observations present in detail the toxicological evaluation of the various ligands, classified into toxicity classes ranging from 3 to 6, where lower numbers indicate higher toxicity. Compounds with LD50 > 2000 mg/kg are safe for biological administration and as potential drugs [55]. Overall, most ligands (L1, L3, L8, L9, L10, L12, L14, and L16) exhibited no

significant toxicity across the evaluated categories, indicating a low likelihood of toxic effects in silico. Despite their predicted high toxicity classifications, ligands L2 and L7 showed no evidence of adverse effects in the applied computational toxicity models. This may be due to their chemical structures, favorable pharmacokinetics, and rapid clearance, all of which reduce toxicity. While predictive tests classified them as non-toxic, harmful effects could still occur under untested conditions, thereby highlighting the need for further studies on their toxicological mechanisms [56].

Table 4. Predicted values for Excretion and Toxicity for the selected compounds (L1–L17) computed using ProTox-II and pkCSM webtools.

	Total Clearance (Log mL/min/kg)	Renal OCT2 Substrate	LD_{50} (mg/kg)	Toxicity Class	Toxicity						
					Immuno	Hepato	Cyto	Carcino	Mutagen	AMES	Skin Sensitization
L1	0.214	No	3400	5	No	No	No	No	No	No	No
L2	2.03	No	750	3	No	No	No	No	No	No	No
L3	1.73	No	5000	5	No	No	No	No	No	No	No
L4	0.92	No	3474	5	No	No	No	Yes	No	No	Yes
L5	1.69	No	5000	5	No	No	No	Yes	No	No	No
L6	0.13	No	6700	6	Yes	No	No	Yes	No	No	No
L7	1.23	No	200	3	No	No	No	No	No	No	No
L8	1.19	No	5000	5	No	No	No	No	No	No	No
L9	1.77	No	5000	5	No	No	No	No	No	No	No
L10	0.26	No	5000	5	No	No	No	No	No	No	No
L11	0.91	No	2000	4	No	No	No	No	No	No	No
L12	1.31	No	4590	5	No	No	No	No	No	No	No
L13	1.79	No	5000	5	No	No	No	No	No	No	Yes
L14	1.06	No	2600	5	No	No	No	No	No	No	No
L15	1.21	No	6700	6	No	No	No	No	Yes	No	No
L16	0.33	No	3000	5	No	No	No	No	No	No	No
L17	1.61	No	2000	4	No	No	No	Yes	No	No	Yes

Ligands L4, L5, L6, and L17 demonstrated potential carcinogenicity, with L6 additionally exhibiting immunotoxic effects, L15 showing mutagenic activity, and L4, L13, and L17 inducing skin sensitization. While L15 and L6 exhibited relatively favorable binding affinities, their predicted toxicological profiles may limit their suitability as lead compounds, necessitating further optimization and experimental validation. Nevertheless, these compounds may still serve as initial scaffolds in drug discovery, provided that appropriate modifications reduce toxicity while maintaining efficacy, with careful benefit–risk assessment guiding any further development. Overall, these findings indicate the need for detailed toxicological studies, including in vivo experiments, along with potential chemical modification or targeted molecular design to lower toxicity while maintaining biological effectiveness. Approaches to reduce toxicity may involve altering functional groups, adjusting dosages, or applying targeted drug delivery methods [29]. Determining each compound's therapeutic window relative to its toxic dose is also essential to ensure safe and effective usage with minimal risk. Although computational toxicity predictions offer valuable preliminary insights, they cannot substitute for thorough experimental studies necessary to establish safety profiles and enable secure therapeutic application. Notably, studies have shown that increased lipophilicity, especially when log P exceeds 3, is strongly linked to higher toxicity risk [39], underscoring the importance of these integrated evaluation strategies.

3.4. Docking Studies for Selected Proteins

The androgen receptor (AR) and CYP17A1 enzyme are central in regulating androgen signaling and synthesis [4], while GSK-3β is closely linked to the metabolic disturbances associated with PCOS, including insulin resistance and inflammation [5]. Given their pivotal roles in the reproductive and metabolic aspects of the syndrome, these proteins were selected for molecular docking studies with compounds derived from *P. harmala* to explore their possible effect on PCOS.

The validation of the docking protocol was achieved through re-docking experiments which yielded RMSD scores below 3 Å, thereby confirming the reliability of the docking methodology with complexes 2AM9, 6WW0, and 1PYX (Table 5). These results indicate that the docking procedure accurately reproduced experimental ligand positions within the binding sites [57]. The binding affinities (ΔG) of the tested compounds, ranging from −5 to −7 kcal/mol, may indicate moderate interactions with the target receptors. Additional parameters such as grid box size, coordinates, ΔG binding energies, and key amino acid interactions of the redocked co-crystalline ligand, are presented in Table 1. The ligands with highest AR affinity are shown within the active site of 2AM9 alongside the redocked native ligand (testosterone, Tes), with zoomed-in views of the binding pocket residues presented in Figure 4A,B. Figure 4C displays contour plots indicating hydrophobicity as well as hydrogen bond acceptor and donor residues in the active site of AR. The molecular docking results of the tested compounds showed that several of them had binding affinities like those of the reference drugs flutamide and nilutamide, which may indicate comparable binding interactions at the computational level. However, these findings are preliminary, as they are based solely on molecular docking results and ADMET predictions. Notably, the studied ligands, as well as the reference drugs, did not exhibit higher binding affinity than Tes, an AR agonist with a ΔG of −11.00 kcal/mol.

Table 5. Affinity energy values (kcal/mol) and RMSD (Å) in molecular docking simulations for selected ligands against selected proteins (PDB: 2AM9, 6WW0 and 1PYX).

Ligand	Target Proteins Binding Affinity (Kcal mol^{-1}) (RMSD in Å)		
	2AM9	**6WW0**	**1PYX**
L3	−7.3 1.83 (Å)	−7 2.81 (Å)	−5.6 1.31 (Å)
L4	−6.4 3.30 (Å)	−6.3 2.99 (Å)	−5.1 2.33 (Å)
L6	−7.5 2.71 (Å)	−7.1 2.60 (Å)	−5.5 0.48 (Å)
L8	−7.1 2.11 (Å)	−6.6 1.73 (Å)	−4.8 2.57 (Å)
L9	−7.00 1.90 (Å)	−6.1 2.38 (Å)	−5.5 0.90 (Å)
L10	−6.9 1.58 (Å)	−7.00 1.71 (Å)	−4.8 2.73 (Å)
L12	−7.00 2.35 (Å)	−6.7 1.79 (Å)	−5.00 1.98 (Å)
L14	−7.7 2.88 (Å)	−7.00 2.34 (Å)	−3.99 4.55 (Å)
L15	−7.9 2.26 (Å)	−7.00 4.02 (Å)	−3.37 4.29 (Å)

Table 5. *Cont.*

Ligand	Target Proteins Binding Affinity (Kcal mol^{-1}) (RMSD in Å)		
	2AM9	**6WW0**	**1PYX**
L16	−6.6 2.99 (Å)	−6.7 2.23 (Å)	−4.60 3.44 (Å)
Flutamide	−7.00 2.01 (Å)	-	-
Nilutamide	−7.8 1.96 (Å)	-	-
I_5	-	-	−7.2 2.29 (Å)
Hymenialdisine (HMD)	-	-	−7.8 1.34 (Å)
Metformin	-	−4.5 1.82 (Å)	-

3: farnesylacetone; **4**: dibutyl phthalate; **6**: beta-calacorene; **8**: 4-(2,6,6-trimethylcyclohexa-1,3-dienyl)but-3-en-2-one; **9**: 4,8,12-Tetradecatrienal, 5,9,13-trimethyl-; **10**: cis-β-damascenone; **12**: beta-Ionone; **14**: dihydroedulan II; **15**: trans-calamenene; **16**: cis-chrysanthenyl acetate. **I_5**: 2-chloro-5-[4-(3-chlorophenyl)-2,5-dioxo-2,5-dihydro-1h-pyrrol-3-ylamino]-benzoic acid.

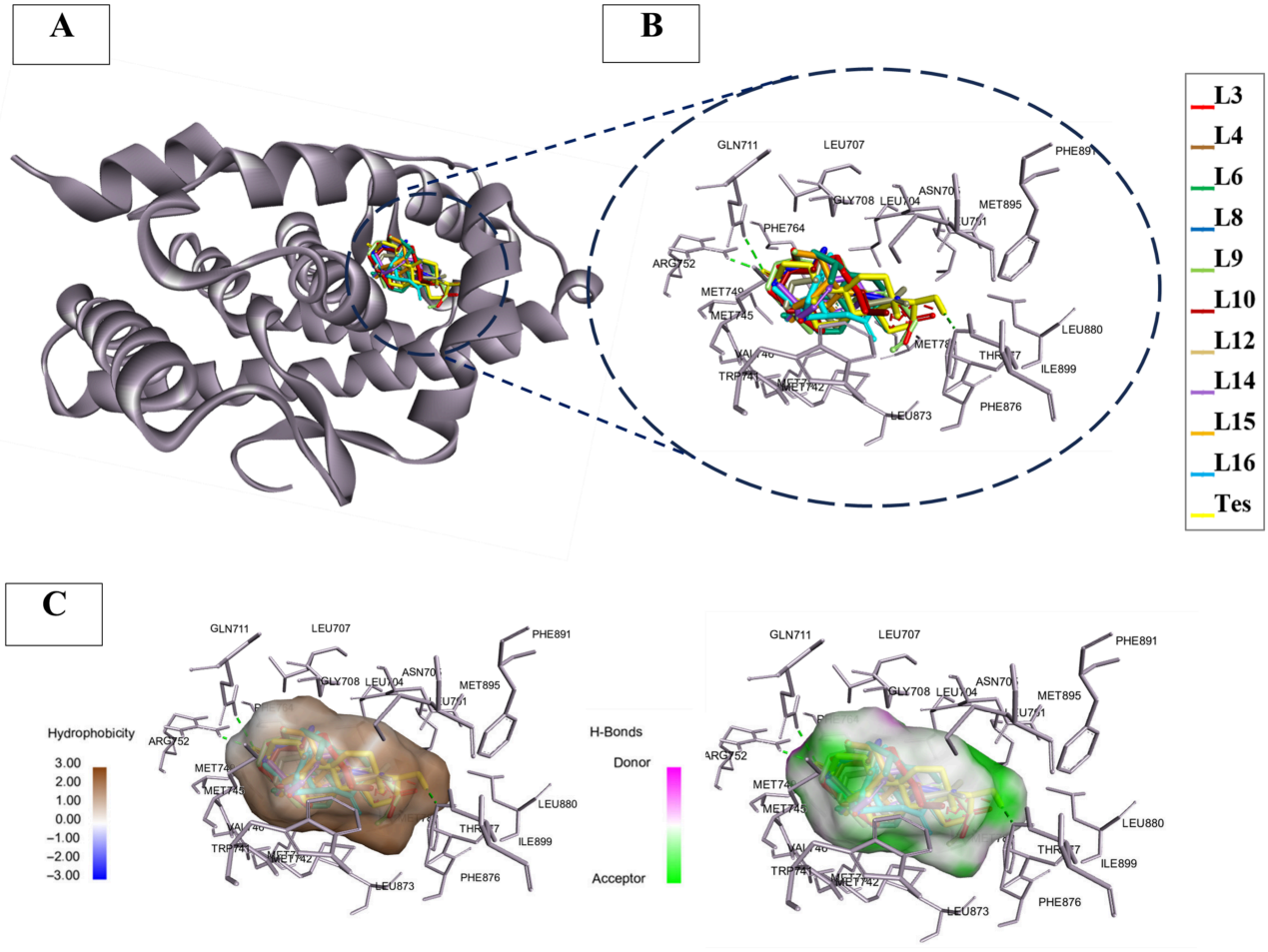


Figure 4. (**A**) Molecular docking of the androgen receptor (PDB: 2AM9). (**B**) Zoom view of the pocket containing the docked ligands: L3, L4, L6, L8, L9, L10, L12, L14, L15, and L16 and for the redocked co-crystalline ligand testosterone (Tes). (**C**) 3D binding modes of hydrogen and hydrophobic interactions between Tes and the pocket of the protein.

As presented in Table 6 and Figure 5, Testosterone forms critical hydrogen bonds with residues such as GLN 711 (-NH to O=C, 2.58 Å) and ARG 752 (-NH to -OH, 2.38 Å), as well as hydrophobic interactions with MET 745 (alkyl interaction at 3.99 Å). These interactions highlight the importance of hydrogen bonds with THR 877, ASN 705, GLN 711, ARG 752, and hydrophobic contacts within the binding pocket, which are known to be essential for high-affinity ligand binding, an observation supported by previous studies [58–60]. Moreover, residues ARG 752 and GLN 711 are recognized as pivotal for ligand stabilization during testosterone binding [61,62]. Among the reference drugs, nilutamide exhibited greater affinity (−7.8 kcal/mol) than flutamide (−7.00 kcal/mol). Figure S1 illustrates that nilutamide forms hydrogen bonds with GLN 711 and engages in hydrophobic interactions with LEU 873 and LEU 707, along with halogen interactions involving LEU 707 and LEU 704, as well as π-sulfur interactions with MET 787. The interactions with flutamide involve hydrogen bonds with HN-GLN 711 and HN-ARG 752 (O. . .N interactions at 2.44 Å and 3.79/3.06 Å, respectively) and hydrophobic alkyl interactions with MET 787 (3.92 Å), with additional halogen bonds involving C-O and O=C groups of residues such as LEU 707, LEU 704, and GLN 711 (distances in the range of 3.17–3.58 Å).

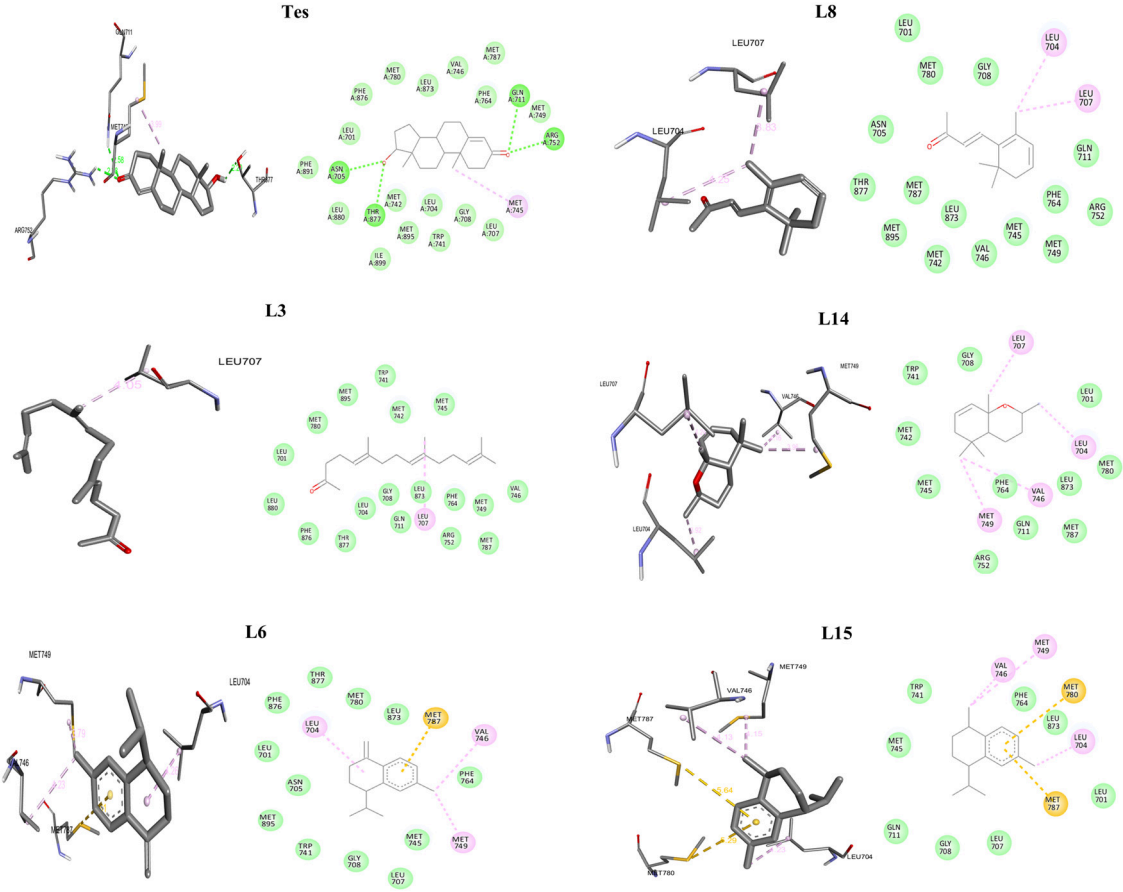


Figure 5. Three- and Two-dimensional interaction diagrams illustrating the binding of native ligand testosterone (Tes) and the investigated ligands Tes, L3, L6, L8, L14, and L15 to the androgen receptor (PDB: 2AM9).

Molecular docking of compounds isolated from *P. harmala* revealed that the ligands interacted within the AR ligand-binding domain primarily through hydrophobic contacts, with additional pi-sulfur interactions involving MET 787 and MET 780 (Figure 5). The results demonstrated that L15 exhibited the strongest binding affinity (−7.9 kcal/mol), although this affinity remains comparable to, and does not exceed, that of testosterone

or reference inhibitors. Moreover, L14 showed a high affinity (−7.7 kcal/mol). Other ligands such as L6, L3, L8, L9, and L12 had slightly lower binding energies suggesting potential binding interactions within the docking model, whereas L10 and L16 displayed the weakest binding among the tested compounds. These interactions were predominantly hydrophobic, as they involved residues such as LEU 704, LEU 707, MET 745, VAL 746, MET 749, ARG 752, PHE 764, and LEU 873 [63]. A previous study highlights the key roles of ARG 752 and GLN 711 in AR ligand binding, which may support their role in ligand recognition [64]. In this context, the docking results for L15, L14, L6, L3, and L8 suggest possible interactions within the AR binding site based on predicted binding affinity from in silico docking.

Table 6. Favorable molecular docking affinity results of the examined compounds against AR (PDB: 2am9).

Ligand	Hydrophobic Interaction (Distance Å)	Others (Distance Å)
L3	Alkyl LEU707 (4.05 Å)	-
L4	-	π-Sulfur: S MET 787 (4.90 Å)
L6	Alkyl: LEU704, VAL746, MET749 (4.26, 4.23, 3.78 Å)	π-Sulfur: S MET 787 (4.61 Å)
L8	Alkyl: LEU 704, LEU 707 (4.24, 3.83 Å)	-
L9	Alkyl: LEU 704 (4.18, 4.08 Å) LEU 707 (4.13 Å), MET 745 (4.30 Å), VAL 746 (4.17 Å)	-
L10	Alkyl: LEU 704, LEU 707, LEU 873 (4.14, 3.93, 4.20 Å)	-
L12	Alkyl: LEU 707, LEU 873 (4.17, 4.00 Å)	-
L14	Alkyl: VAL 746, MET 749, LEU 707, LEU 704 (4.16, 3.96, 4.24, 3.92 Å)	-
L15	Alkyl: VAL 746, MET 749, LEU 704 (4.13, 4.14, 4.23 Å)	π-Sulfur: S MET 780, MET 787 (5.29, 5.64 Å)
L16	Alkyl: VAL746, MET749, LEU704 (4.01, 3.85, 3.99 Å)	-

3: farnesylacetone; 4: dibutyl phthalate; 6: β-calacorene; 8: 4-(2,6,6-trimethylcyclohexa-1,3-dienyl)but-3-en-2-one; 9: 4,8,12-tetradecatrienal, 5,9,13-trimethyl-; 10: cis-β-damascenone; 12: β-ionone; 14: dihydroedulan II; 15: trans-calamenene; 16: cis-chrysanthenyl acetate.

Results from the molecular docking of ten compounds and the analog ligand, 3-keto-5α-abiraterone (UDJ) targeting the steroid 17α-hydroxylase/17,20-lyas (CYP17A1) structure (PDB ID: 6WW0), are summarized in Table 5. The ligands with the strongest binding affinities are collectively shown within the active site of 6WW0, with the re-docked UDJ also illustrated in Figure 6A. Figure 6B provides an enlarged view of the residues present in the pocket of the docked UDJ. Moreover, Figure 6C presents contour maps emphasizing the hydrophobic regions and the locations of hydrogen bond acceptors and donor residues within the active site of CYP17A1. However, none of these ligands outperformed the analog ligand UDJ, which exhibited a binding affinity of −10.9 kcal/mol and an RMSD of 1.65 Å. Notably, as shown in Figure 7 and Table 7, the UDJ ligand formed a key hydrogen bond between the amino group (-NH) of ASN 202 and the carbonyl oxygen (O=C), with a bond length of 2.06 Å, contributing to the stabilization of the complex.

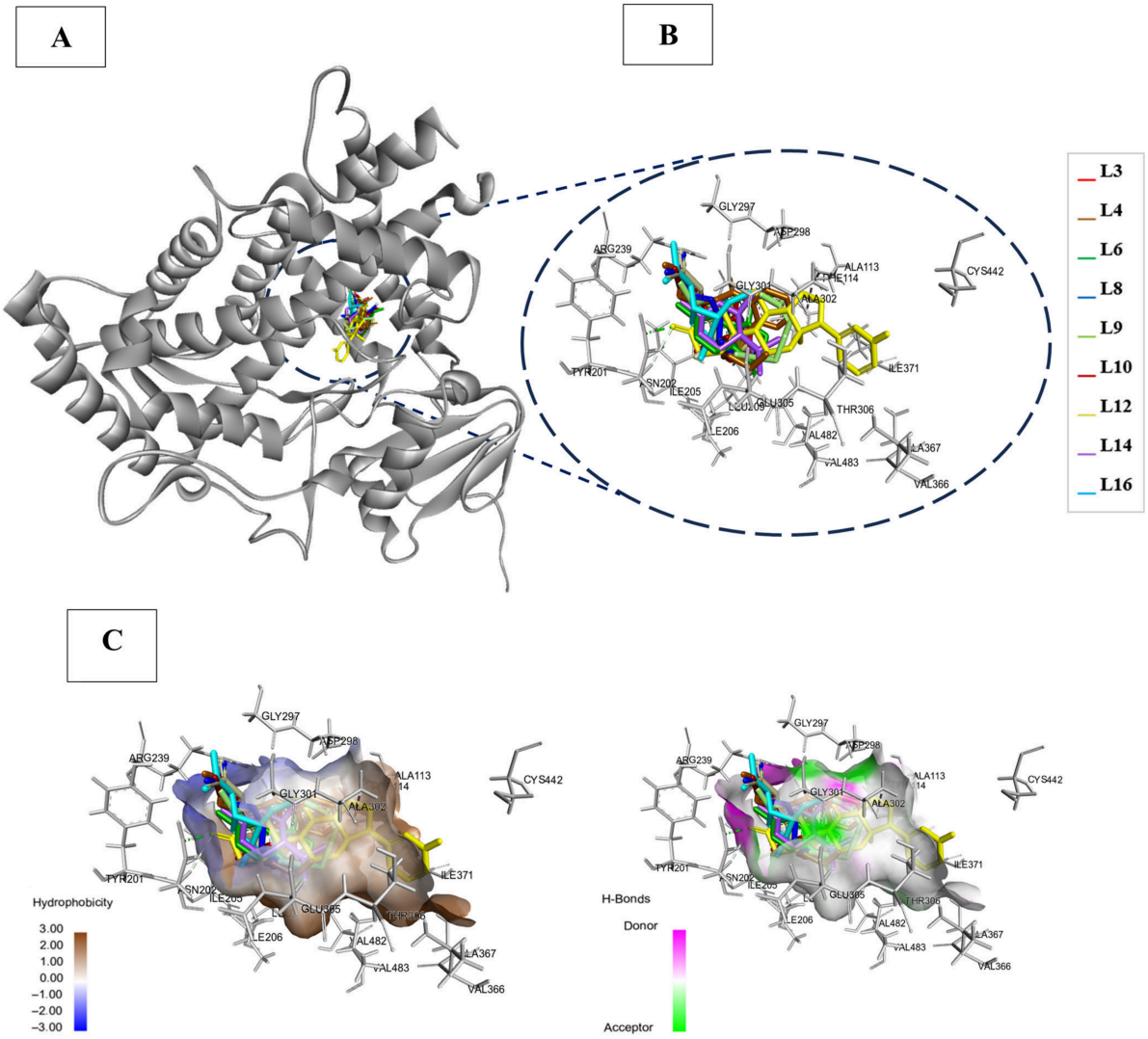


Figure 6. (**A**) Molecular docking of human steroidogenic cytochrome P450 17A1 (PDB: 6WW0). (**B**) Zoom view of the pocket containing the docked ligands: L3, L4, L6, L8, L9, L10, L12, L14, L16 and the redocked co-crystalline ligand 3-keto-5alpha-abiraterone (UDJ). (**C**) 3D Binding modes of hydrogen and hydrophobic interactions between UDJ and the pocket of the protein.

Table 7. Favorable molecular docking affinity results of the examined compounds against (PDB: 6WW0).

Ligand	Hydrogen Bonds (Distance Å)	Hydrophobic Interaction (Distance Å)	Electrostatic (Distance Å)
L3	Conventional Hydrogen bonds: SC D-H: HN- ASN 202 to O=C (2.50 Å)	Alkyl: ALA 105, VAL 482, ILE 205 (4.21, 4.20, 3.75Å)	-
L4	Conventional Hydrogen bonds: SC D-H: HN- ARG 239 To O=C-O (2.39 Å) Carbon-Hydrogen bond: SC D-H: H-C- GLY 301 To O=C-O (3.71 Å)	-	Electrostatic: π-Anion; O-C- ASP 298 (4.42 Å)
L6	-	Alkyl: VAL 284, ALA 105 (3.89, 4.19 Å)	-
L8	Conventional Hydrogen bonds: SC D-H: HN- ARG 239 To O=C (2.08 Å)	Alkyl: ALA 105, ILE 205 (3.79, 3.89 Å)	-

Table 7. *Cont.*

Ligand	Hydrogen Bonds (Distance Å)	Hydrophobic Interaction (Distance Å)	Electrostatic (Distance Å)
L9	Conventional Hydrogen bonds: SC D-H: HN- ARG 239 To O=C (2.33 Å)	Alkyl: ALA 105, ALA 113 (3.66 Å, 3.78 Å) π-Alkyl: PHE 114 (4.27 Å)	-
L10	-	Alkyl: ALA 105, ILE 205 (3.78, 3.81 Å)	-
L12	Conventional Hydrogen bonds: SC D-H: HN- ARG 239 To O=C (2.11 Å)	Alkyl: ALA 105, ILE 205 (3.51, 4.11 Å)	-
L14	-	Alkyl: ALA 302, ILE 205 (3.80, 3.67 Å)	-
L16	Conventional Hydrogen bonds: SC D-H: 2 HN- ASN 202 To O=C (2.24 Å) SC D-H: HN- ARG 239 To -O- (3.03 Å)	-	-

3: farnesylacetone; 4: dibutyl phthalate; 6: β-calacorene; 8: 4-(2,6,6-trimethylcyclohexa-1,3-dienyl)but-3-en-2-one; 9: 4,8,12-tetradecatrienal, 5,9,13-trimethyl-; 10: cis-β-damascenone; 12: β-ionone; 14: dihydroedulan II; 16: cis-chrysanthenyl acetate; SC: side chain, D-H: hydrogen donor.

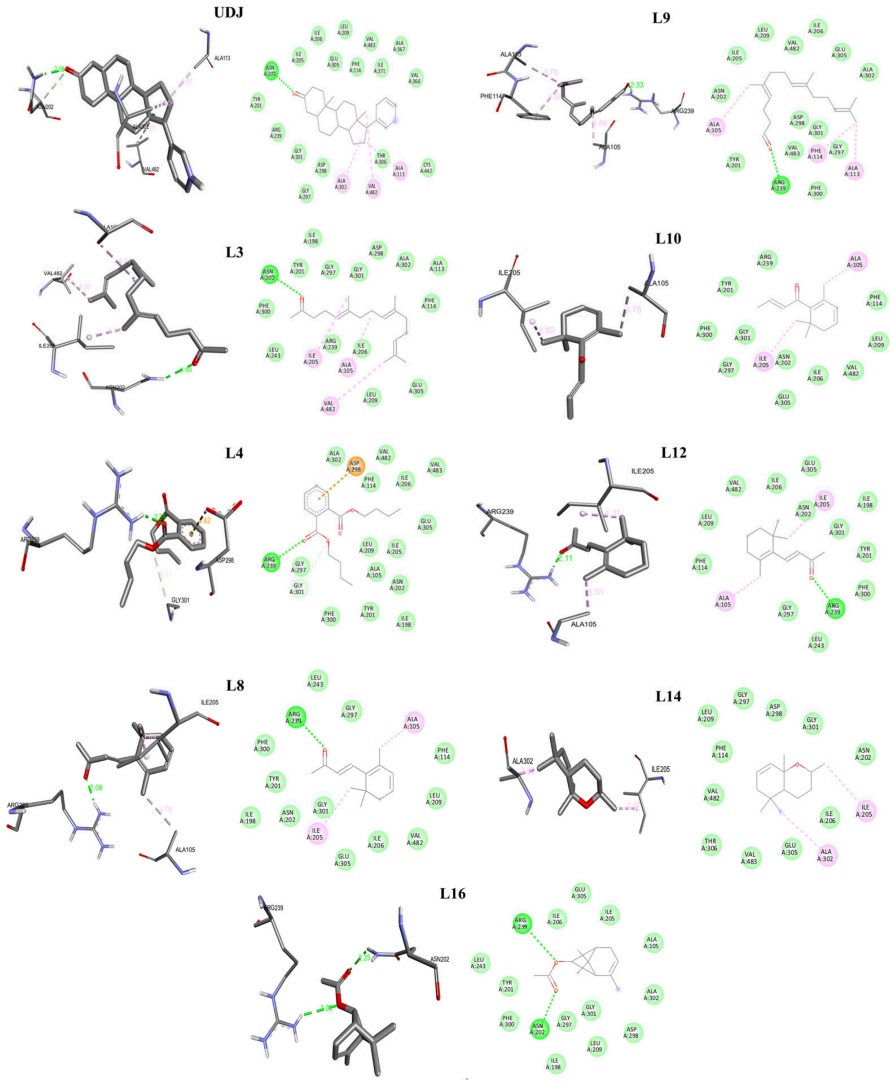


Figure 7. Three- and Two-dimensional interaction diagrams illustrating the binding of human steroidogenic cytochrome P450 17A1 (PDB: 6WW0) and the investigated ligands UDJ, L3, L4, L8, L9, L10, L12 L14, and L16.

Additionally, a carbon-hydrogen bond between a hydrogen atom and the oxygen atom of ASN 202 oxygen at 3.53 Å, along with hydrophobic interactions involving residues ALA 113, ALA 302, and VAL 482 at distances of 3.97 Å, 3.66 Å, and 4.27 Å, respectively, stabilized the ligand within the active site. These interactions collectively suggest a stable binding mode within the docking framework, mainly through hydrogen bonding and hydrophobic contacts. Previously, it was reported that an intermolecular hydrogen bond involving the ligand occurs between the 3β-hydroxyl group of abiraterone and ASN 202 within the CYP17A1 active site [65–68], a residue critical for substrate binding and specificity [6]. Other key residues contributing to the architecture of the pocket include ARG 239 which formed hydrogen bonds with various ligands, and the hydrophobic wall comprising residues such as ALA 105, SER 106, and PHE 114 which shape the active site and influence substrate accommodation [69,70]. Additional polar residues such as GLU 305 and ASP 298, although not directly interacting with abiraterone or galeterone, may be relevant for designing non-steroidal inhibitors [71]. Among the tested ligands, L6 showed a strong binding affinity of −7.1 kcal/mol, with an RMSD of 2.60 Å, engaging in alkyl interactions with VAL 284 and ALA 105. Similar binding energies (−7.00 kcal/mol) and RMSD values below 3 Å were observed for L3, L10 and L14. Specifically, L3 formed a hydrogen bond (2.50 Å) with ASN 202, in addition to hydro-phobic contacts with ALA 105, ILE 205, and VAL 482. In contrast, L10 interacted solely through alkyl contacts with ALA 105 and ILE 205, whereas L14 interacted with ALA 302 and ILE 205. Although L15 also demonstrated a binding affinity of −7.00 kcal/mol, its RMSD exceeded 3 Å, and it engaged only in alkyl interactions with ILE 205. In comparison, L16 showed an affinity of −6.7 kcal/mol with RMSD of 2.33 Å and formed two hydrogen bonds with ASN 202 and ARG 239, along with hydrophobic interactions. Similarly, L12 exhibited an affinity of −6.7 kcal/mol and an RMSD of 1.79 Å, forming a hydrogen bond with ARG 239, while L8 had a binding affinity of −6.6 kcal/mol, with RMSD of 1.73 Å, interacting via hydrophobic contacts with ALA 105 and ILE 205, in addition to hydrogen bonds with ARG 239. With a binding affinity of −6.3 kcal/mol and RMSD 2.99 Å, L4 formed hydrogen bonds with ARG 239 carboxyl group and a C–H bond with GLY 301, in addition to π–anion electrostatic interactions with ASP 298. Ligand L9 demonstrated an affinity of −6.1 kcal/mol and RMSD of 2.38 Å; it formed a hydrogen bond with ARG 239 and π-alkyl interactions with ALA 105, ALA 113, and PHE 114. Metformin, included as a comparative reference [34,72], showed a lower binding affinity (−4.5 kcal/mol, RMSD: 1.82 Å), forming hydrogen bonds with ASP 298 and GLY 297, along with a C–H interaction with ASN 202 [73]. The ligands L3, L10, and L16 demonstrated relatively favorable binding interactions within the docking framework, interacting with key active-site residues such as ASN 202, VAL 284, and ARG 239, which are crucial for substrate recognition and catalytic activity. Overall, the results indicate moderate binding interactions within the CYP17A1 active site based on molecular docking studies; however, these findings remain hypothetical and require experimental validation, without evidence of functional or physiological effect [6]. The predicted binding modes further suggest that these ligands may occupy the enzyme's active site.

GSK-3β is a kinase involved in cellular signaling and metabolic pathways that have been reported to be associated with PCOS pathophysiology [5]. Molecular docking analysis of GSK-3β (PDB ID: 1PYX) revealed varying binding affinities and interaction patterns for the tested ligands, as summarized in Table 5. In addition, an enlarged view of the residues forming the binding pocket of the docked ATP analog AMP-PNP is presented in Figure 8A,B. Additionally, Figure 8C displays contour maps illustrating the hydrophobic regions and the positions of hydrogen bond donor and acceptor residues within the 1PYX active site. Among the compounds, L3 and L9 demonstrated the highest binding affinities, with values of −5.6 and −5.5 kcal/mol, respectively, and RMSD values of 1.31 Å and

0.90 Å, respectively. Notably, as shown in Figure 9 and Table 8, Ligand L3 formed hydrogen bonds between the HN-group of LYS 183 and O=C (3.05 and 2.98 Å), and between HN− of GLN 185 and O=C (2.55 Å), along with hydrophobic interactions with ILE 62 (3.87 Å). Similarly, L9 formed three hydrogen bonds: between HN− of LYS 183 and O=C (3.02 and 3.01 Å), between HN− of GLN 185 and O=C (2.62 Å), and hydrophobic interactions with ILE 62 (3.89 Å). Ligand L6 had a binding affinity of −5.5 kcal/mol, with RMSD of 0.481 Å; it formed a non-covalent interaction between the positively charged -NH group of ARG 141 and the electron-rich π-system of an aromatic ring in the ligand (4.08 Å). For L4, it had a binding affinity of −5.1 kcal/mol and an RMSD of 2.33 Å, and it formed two H-bonds between HN− of ARG 141 and O=C (2.39 and 2.54 Å), one carbon-hydrogen bond between HC-ARG 141 and O=C (3.29 Å), and a hydrophobic pi-sigma interaction with ILE 62 (3.95 Å). With a binding affinity of −5.00 kcal/mol and RMSD of 1.981 Å, L12 did not form hydrogen bonds but exhibited a hydrophobic π-alkyl interaction with TYR 140 (4.14 Å). Compounds L8, L10, L14, L15, and L16 demonstrated relatively weaker binding affinities (<5 kcal/mol).

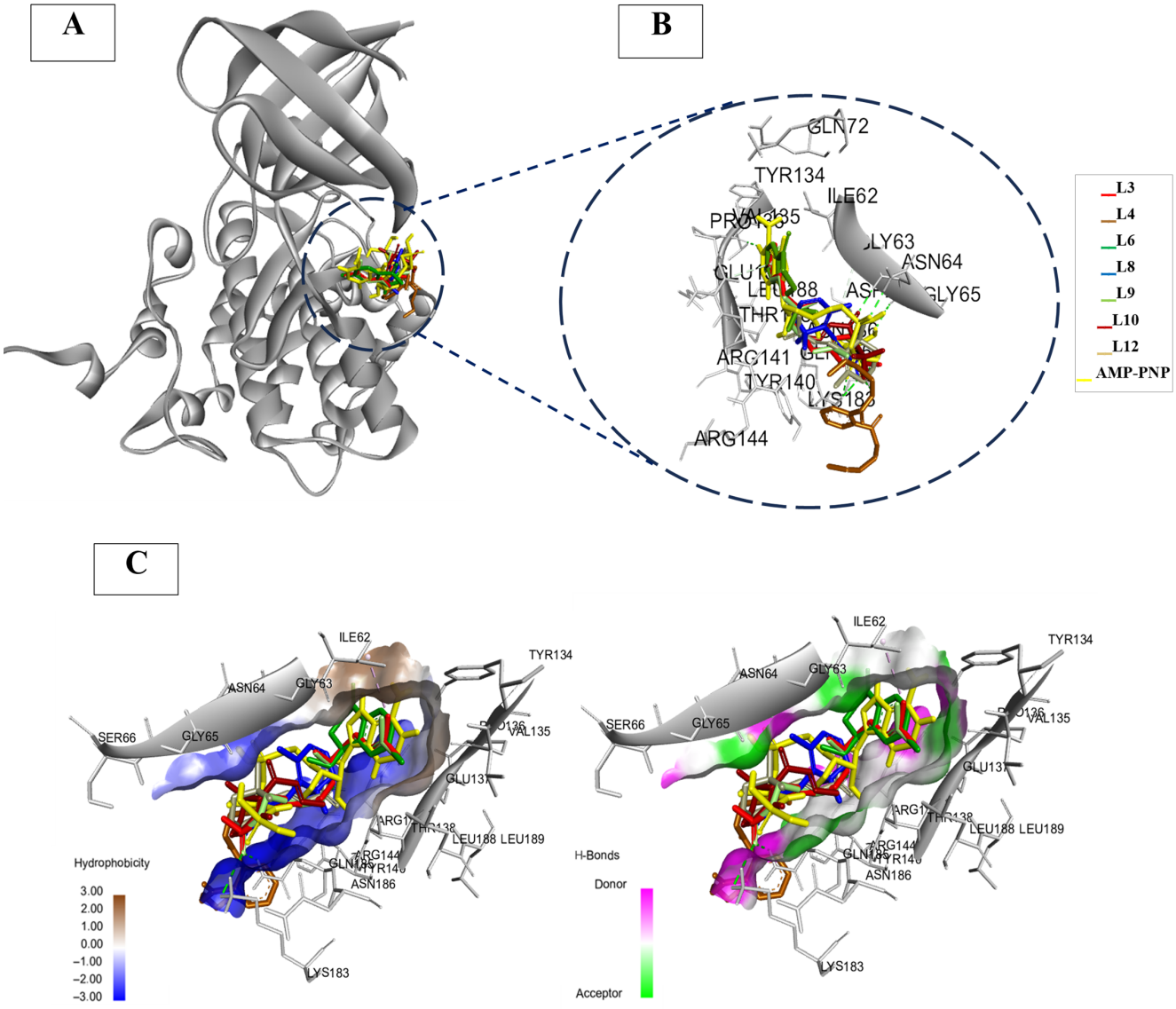


Figure 8. (**A**) Molecular docking of glycogen synthase kinase 3-beta (PDB: 1PYX). (**B**) Zoomed-in view of the pocket containing the docked ligands: L3, L4, L6, L8, L9, L10, L12 and the redocked co-crystalline ligand adenylyl imidodiphosphate (AMP-PNP). (**C**) 3D binding modes of hydrogen and hydrophobic interactions between AMP-PNP and the pocket of the protein.

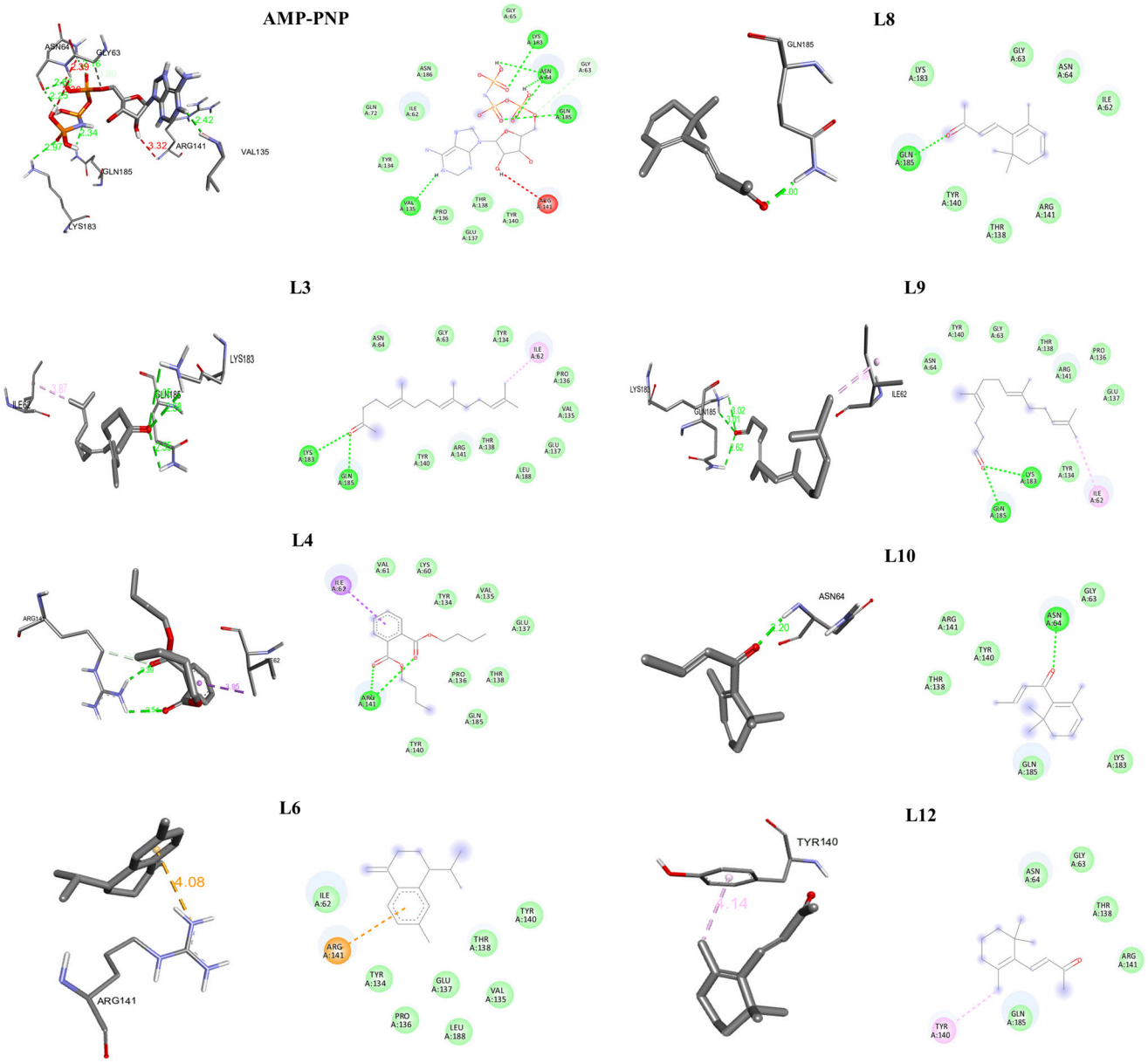


Figure 9. Three- and Two-dimensional interaction diagrams illustrating the binding of glycogen synthase kinase 3 beta (PDB: 1PYX) and the investigated ligands AMP-PNP, L3, L4, L6, L8, L9, L10, and L12.

Comparing these results with the redocking of the crystallized ATP analog AMP-PNP to GSK-3β (PDB ID: 1PYX), which served as the baseline, AMP-PNP exhibited a binding affinity of −7.6 kcal/mol and an RMSD of 1.95 Å. The interactions of AMP-PNP were predominantly characterized by hydrogen bonds and hydrophobic contacts. Specifically, several hydrogen bonds were observed, such as those between the side chain O=C of ASN 64 and HO-groups at distances of 2.62 Å and 2.25 Å, respectively, and between the HN-group of ASN 64 and O=P at 2.16 Å. Additional hydrogen bonds involved the O=C group of VAL 135 with HN− (2.42 Å), HN− of GLN 185 with O=C (2.34 Å), and HN− of LYS 183 with O=C (2.97 Å), as well as a carbon-hydrogen bond between HC-GLY 63 and O-P at 3.80 Å. These interactions, as previously characterized, were within the ATP-binding pocket of GSK-3β [74]. It has been noted that the key residues ASP 133, VAL 135, GLU 137, ARG 141, GLN 185, ASP 200, and ARG 220, are critical for the interactions at the ATP-binding pocket [75]. Likewise, Figure S3 shows the ATP-competitive inhibitor, I-5,

which exhibited a binding affinity of −7.2 kcal/mol and RMSD of 2.29 Å. It formed three hydrogen bonds: the first between the side chain -NH of ARG 141 and the carbonyl oxygen of I-5 (2.66 Å), the second between the backbone carbonyl of ILE 62 and the HN− group of I-5 (2.17 Å), and the third between the side chain HN− of ASN 64 and the oxygen atom of the -COO group in I-5 (1.98 Å). In addition, a favorable electrostatic interaction occurred between the side chain amine of ARG 141 and the electron-rich π-system of the aromatic ring of I-5 (4.27 Å), thereby reinforcing its stable interaction within the ATP-binding pocket of GSK-3β, which is consistent with previous findings [74–76].

Table 8. Favorable molecular docking affinity results of the examined compounds against (PDB: 1PYX).

Ligand	Hydrogen Bonds (Distance Å)	Hydrophobic Interaction (Distance Å)	Electrostatic Interactions (Distance Å)
L3	Conventional Hydrogen bonds: SC D-H: HN- LYS 183 to O=C (3.05, 2.98 Å) SC D-H: HN- GLN 185 to O=C (2.55 Å)	Alkyl: IL 62 (4.21, 4.20, 3.75Å)	-
L4	Conventional Hydrogen bonds: SC D-H: HN- ARG 141 to O=C (2.39, 2.54 Å) Carbon-Hydrogen bond: SC D-H: HC- ARG 141 to O=C (3.29 Å)	π-Sigma: IL 62 (3.95 Å)	-
L6	-	-	A non-covalent attraction between a positively charged ion (NH) in ARG 141 and the electron-rich π system of an aromatic ring in the ligand (4.08 Å)
L8	Conventional Hydrogen bonds: SC D-H: HN- GLN 185 to O=C (2.00 Å)	-	-
L9	Conventional Hydrogen bonds: SC D-H: HN- GLN 185 to O=C (2.62 Å) SC D-H: HN- LYS 183 to O=C (3.02, 3.01Å)	Alkyl: LEU 62 (3.89 Å)	-
L10	Conventional Hydrogen bonds: SC D-H: HN- ASN 64 to O=C (2.20 Å)		-
L12	-	π-Alkyl: TYR140 (4.14 Å)	-

3: farnesylacetone; 4: dibutyl phthalate; 6: β-calacorene; 8: 4-(2,6,6-trimethylcyclohexa-1,3-dienyl)but-3-en-2-one; 9: 4,8,12-tetradecatrienal, 5,9,13-trimethyl-; 10: cis-β-damascenone; 12: β-ionone; SC: Side chain; D-H: Hydrogen donor.

The ATP-competitive inhibitor hymenialdisine (HMD) exhibited a binding affinity of −7.8 kcal/mol and an RMSD of 1.338 Å (Figure S3). It formed three hydrogen bonds: two between the O=C group and H−N group of VAL 135 (2.21 Å and 2.32 Å), one between O=C group and H−O group of TYR 134 (2.13 Å), and a C–H interaction with ILE 62 (3.33 Å). Structural analysis has demonstrated that residues such as ASP 133, VAL 135, THR 138, and GLN 185 participate in hydrogen bonding and electrostatic interactions with ARG 141 and the inhibitor in nearly all co-crystals of ATP-competitive inhibitors with GSK-3β. The hydrophobic pocket of the ATP-binding domain formed by ILE 62, VAL 70, ALA 83, and LEU 188, as well as the complementary hinge segment consisting of LEU 132, ASP 133, TYR 134, VAL 135 and PRO 136, play critical roles in stabilizing the interaction [77]. In summary, the tested ligands showed weaker binding affinities than AMP-PNP, I-5, and HMD, with L3, L9, and L6 displaying comparatively favorable interactions. The remaining

compounds showed limited binding performance, suggesting reduced inhibitory potential as standalone agents. These findings provide insight into binding behavior and support further optimization to enhance affinity and inhibitory activity against GSK-3β.

4. Conclusions

This study highlights *Peganum harmala* (*P. harmala*) as a source of bioactive compounds with predicted binding affinity toward selected molecular targets associated with polycystic ovary syndrome (PCOS). A subset of identified terpenoid derivatives, including farnesylacetone (L3), β-calacorene (L6), dihydroedulan II (L14), trans-calamenene (L15), cis-β-damascenone (L10), cis-chrysanthenyl acetate (L16), and related oxygenated hydrocarbons, showed favorable physicochemical properties supporting drug-likeness potential. In silico pharmacokinetic analysis indicated acceptable gastrointestinal absorption, limited blood–brain barrier permeability, and manageable cytochrome P450 (CYP450) enzyme interaction profiles, with an overall acceptable preliminary safety profile. Molecular docking analysis showed that several compounds, particularly L15, L14, L6, L3, and L8, exhibited relatively higher binding affinities toward the androgen receptor (AR), indicating favorable ligand–receptor interactions within the binding site. In addition, L3, L10, and L16 showed predicted interactions with Steroid 17α-hydroxylase/17,20-lyase (CYP17A1), a key enzyme in androgen biosynthesis, while L3, L6, and L9 demonstrated comparatively stronger binding to glycogen synthase kinase-3β (GSK-3β), which is implicated in metabolic dysregulation associated with PCOS. These findings are based on computational predictions and should be interpreted as hypothesis-generating evidence for potential multi-target interactions relevant to polycystic ovary syndrome (PCOS). The observed binding patterns suggest interaction tendencies that warrant further experimental validation. Among the evaluated compounds, L3, L6, L14, and L15 emerged as the top-ranked lead candidates across the analyzed targets, reflecting more favorable and consistent in silico performance profiles. The integrated *in silico* analysis provides a mechanistic rationale for prioritizing selected *P. harmala* constituents for future investigation. Further in vitro and in vivo studies are necessary to validate their biological activity, pharmacokinetic behavior, and safety profiles.

Supplementary Materials: The following supporting information can be downloaded at: https://www.mdpi.com/article/10.3390/app16094214/s1, Table S1: GC-MS analysis of P. harmala leaves; Figure S1: Three and Two-dimensional interaction diagrams illustrating the binding of reference drugs (A) flutamide and (B) nilutamide to the AR protein (PDB: 2AM9); Figure S2: Three and Two-dimensional interaction diagrams illustrating the binding of inhibitors (A) I-5 and (B) HMD to the human steroidogenic cytochrome P450 17A1 (PDB: 6WW0); Figure S3: Two-dimensional interaction diagrams illustrating the binding of the reference drug metformin to the glycogen synthase kinase 3 beta (PDB: 1PYX).

Author Contributions: W.A.A.-O. and S.M.A. contributed equally. All authors have read and agreed to the published version of the manuscript.

Funding: This research received no external funding.

Institutional Review Board Statement: Not applicable.

Informed Consent Statement: Not applicable.

Data Availability Statement: The original contributions presented in this study are included in the article. Further inquiries can be directed to the corresponding author.

Conflicts of Interest: The authors declare that they have no known competing financial interests or personal relationships that could have appeared to influence the work reported in this paper.

References

1. Houston, E.J.; Templeman, N.M. Reappraising the relationship between hyperinsulinemia and insulin resistance in PCOS. *J. Endocrinol.* **2025**, *265*, e240269. [CrossRef]
2. Almhmoud, H.; Alatassi, L.; Baddoura, M.; Sandouk, J.; Alkayali, M.Z.; Najjar, H.; Zaino, B. Polycystic ovary syndrome and its multidimensional impacts on women's mental health: A narrative review. *Medicine* **2024**, *103*, e38647. [CrossRef] [PubMed]
3. Deng, H.; Chen, Y.; Xing, J.; Zhang, N.; Xu, L. Systematic low-grade chronic inflammation and intrinsic mechanisms in polycystic ovary syndrome. *Front. Immunol.* **2024**, *15*, 1470283. [CrossRef] [PubMed]
4. Ye, W.; Xie, T.; Song, Y.; Zhou, L. The role of androgen and its related signals in PCOS. *J. Cell. Mol. Med.* **2021**, *25*, 1825–1837. [CrossRef] [PubMed]
5. Wang, K.; Li, Y. Signaling pathways and targeted therapeutic strategies for polycystic ovary syndrome. *Front. Endocrinol.* **2023**, *14*, 1191759. [CrossRef] [PubMed]
6. Gregory, M.C.; Mak, P.J.; Khatri, Y.; Kincaid, J.R.; Sligar, S.G. Human P450 CYP17A1: Control of substrate preference by asparagine 202. *Biochemistry* **2018**, *57*, 764–771. [CrossRef]
7. Domecq, J.P.; Prutsky, G.; Mullan, R.J.; Sundaresh, V.; Wang, A.T.; Erwin, P.J.; Welt, C.; Ehrmann, D.; Montori, V.M.; Murad, M.H. Adverse Effects of the Common Treatments for Polycystic Ovary Syndrome: A Systematic Review and Meta-Analysis. *J. Clin. Endocrinol. Metab.* **2013**, *98*, 4646–4654. [CrossRef] [PubMed]
8. Al Akeel, M.M.; Al Ghamdi, W.M.; Al Habib, S.; Koshm, M.; Al Otaibi, F. Herbal medicines: Saudi population knowledge, attitude, and practice at a glance. *J. Fam. Med. Prim. Care* **2018**, *7*, 865–875. [CrossRef]
9. Sharifi-Rad, J.; Quispe, C.; Herrera-Bravo, J.; Semwal, P.; Painuli, S.; Özçelik, B.; Hacıhasanoğlu, F.E.; Shaheen, S.; Sen, S.; Acharya, K.; et al. *Peganum* spp.: A Comprehensive Review on Bioactivities and Health-Enhancing Effects and Their Potential for the Formulation of Functional Foods and Pharmaceutical Drugs. *Oxidative Med. Cell. Longev.* **2021**, *2021*, 5900422. [CrossRef]
10. Marwat, S.K.; ur Rehman, F. Medicinal and pharmacological potential of harmala (*Peganum harmala* L.) seeds. In *Nuts and Seeds in Health and Disease Prevention*; Elsevier: Amsterdam, The Netherlands, 2011; pp. 585–599.
11. Abdelsattar, M.; Elseady, Y.; Hendawy, A.; Diab, A.E.-A.A.; Awadin, W.F.; Eldesoqui, M. Impact of *Peganum harmala*/Zinc Oxide Nanoparticles on Thyroid and Pancreatic Function in Obese Rats: A Biochemical and Physiological Analysis. *Int. J. Pharmacol.* **2024**, *20*, 981–990. [CrossRef]
12. Abbas, M.W.; Hussain, M.; Qamar, M.; Ali, S.; Shafiq, Z.; Wilairatana, P.; Mubarak, M.S. Antioxidant and anti-inflammatory effects of *Peganum harmala* extracts: An in vitro and in vivo study. *Molecules* **2021**, *26*, 6084. [CrossRef]
13. Li, L.-N. *Peganum harmala* L.: A review of botany, traditional use, phytochemistry, pharmacology, quality marker, and toxicity. *Comb. Chem. High Throughput Screen.* **2024**, *27*, 797–822. [CrossRef]
14. Moloudizargari, M.; Mikaili, P.; Aghajanshakeri, S.; Asghari, M.H.; Shayegh, J. Pharmacological and therapeutic effects of *Peganum harmala* and its main alkaloids. *Pharmacogn. Rev.* **2013**, *7*, 199–212. [CrossRef]
15. Kilic, O.; Sahin, T.; Sahan, Z. Biochemical properties and nutritional importance of some medicinal and aromatic plants. In *Bioactive Components and Biochemical Properties in Foods*; Orient Yayınları: Ankara, Turkey, 2025; p. 66.
16. Apostolico, I.; Aliberti, L.; Caputo, L.; De Feo, V.; Fratianni, F.; Nazzaro, F.; Souza, L.F.; Khadhr, M. Chemical composition, antibacterial and phytotoxic activities of *Peganum harmala* seed essential oils from five different localities in Northern Africa. *Molecules* **2016**, *21*, 1235. [CrossRef]
17. Yang, S.; Bai, M.; Yang, J.; Yuan, Y.; Zhang, Y.; Qin, J.; Kuang, Y.; Sampietro, D.A. Chemical composition and larvicidal activity of essential oils from *Peganum harmala*, *Nepeta cataria* and *Phellodendron amurense* against *Aedes aegypti* (Diptera: Culicidae). *Saudi Pharm. J.* **2020**, *28*, 560–564. [CrossRef]
18. Selim, S.; Aziz, M.; Mashait, M.; Warrad, M. Antibacterial activities, chemical constitutes and acute toxicity of Egyptian *Origanum majorana* L., *Peganum harmala* L. and *Salvia officinalis* L. essential oils. *Afr. J. Pharm. Pharmacol.* **2013**, *7*, 725–735.
19. Wang, Y.; Liu, H.; Yu, S.; Zhang, Y.; Huang, Y.; He, X.; Chen, W. Effects of geographical, soil and climatic factors on the two marker secondary metabolites contents in the roots of *Rubia cordifolia* L. *Front. Plant Sci.* **2024**, *15*, 1419392. [CrossRef] [PubMed]
20. Xu, J.; Xie, J.; Zhang, M.; Lin, J. Pharmacological effects of Chinese herbal active compounds in the intervention of polycystic ovary syndrome: Focusing on molecular mechanisms. *All Life* **2026**, *19*, 2612407. [CrossRef]
21. Kim, S.; Chen, J.; Cheng, T.; Gindulyte, A.; He, J.; He, S.; Li, Q.; Shoemaker, B.A.; Thiessen, P.A.; Yu, B.; et al. PubChem 2019 update: Improved access to chemical data. *Nucleic Acids Res.* **2019**, *47*, D1102–D1109. [CrossRef] [PubMed]
22. Wishart, D.S.; Feunang, Y.D.; Guo, A.C.; Lo, E.J.; Marcu, A.; Grant, J.R.; Sajed, T.; Johnson, D.; Li, C.; Sayeeda, Z.; et al. DrugBank 5.0: A major update to the DrugBank database for 2018. *Nucleic Acids Res.* **2018**, *46*, D1074–D1082. [CrossRef]
23. Adedotun, I.O.; Abdul-Hammed, M.; Hamzat, B.A.; Adepoju, A.J.; Akinboade, M.W.; Afolabi, T.I.; Ismail, U.T. Molecular docking, ADMET analysis, and bioactivity studies of phytochemicals from *Phyllanthus niruri* as potential inhibitors of hepatitis C virus NSB5 polymerase. *J. Indian Chem. Soc.* **2022**, *99*, 100321. [CrossRef]

24. Hasan, M.M.; Khan, Z.; Chowdhury, M.S.; Khan, M.A.; Moni, M.A.; Rahman, M.H. In silico molecular docking and ADME/T analysis of Quercetin compound with its evaluation of broad-spectrum therapeutic potential against particular diseases. *Inform. Med. Unlocked* **2022**, *29*, 100894. [CrossRef]
25. Waterhouse, A.; Bertoni, M.; Bienert, S.; Studer, G.; Tauriello, G.; Gumienny, R.; Heer, F.T.; de Beer, T.A.P.; Rempfer, C.; Bordoli, L.; et al. SWISS-MODEL: Homology modelling of protein structures and complexes. *Nucleic Acids Res.* **2018**, *46*, W296–W303. [CrossRef] [PubMed]
26. Trott, O.; Olson, A.J. AutoDock Vina: Improving the speed and accuracy of docking with a new scoring function, efficient optimization, and multithreading. *J. Comput. Chem.* **2010**, *31*, 455–461. [CrossRef]
27. Wang, Y.; Xiao, J.; Suzek, T.O.; Zhang, J.; Wang, J.; Bryant, S.H. PubChem: A public information system for analyzing bioactivities of small molecules. *Nucleic Acids Res.* **2009**, *37*, W623–W633. [CrossRef]
28. Singh, D.B.; Gupta, M.K.; Singh, D.V.; Singh, S.K.; Misra, K. Docking and in silico ADMET studies of noraristeromycin, curcumin and its derivatives with Plasmodium falciparum SAH hydrolase: A molecular drug target against malaria. *Interdiscip. Sci.* **2013**, *5*, 1–12. [CrossRef] [PubMed]
29. Daina, A.; Michielin, O.; Zoete, V. SwissADME: A free web tool to evaluate pharmacokinetics, drug-likeness and medicinal chemistry friendliness of small molecules. *Sci. Rep.* **2017**, *7*, 42717. [CrossRef]
30. Lipinski, C.A. Lead- and drug-like compounds: The rule-of-five revolution. *Drug Discov. Today Technol.* **2004**, *1*, 337–341. [CrossRef]
31. Khan, M.T. Predictions of the ADMET properties of candidate drug molecules utilizing different QSAR/QSPR modelling approaches. *Curr. Drug Metab.* **2010**, *11*, 285–295. [CrossRef]
32. Banerjee, P.; Eckert, A.O.; Schrey, A.K.; Preissner, R. ProTox-II: A webserver for the prediction of toxicity of chemicals. *Nucleic Acids Res.* **2018**, *46*, W257–W263. [CrossRef]
33. Pires, D.E.; Blundell, T.L.; Ascher, D.B. pkCSM: Predicting small-molecule pharmacokinetic and toxicity properties using graph-based signatures. *J. Med. Chem.* **2015**, *58*, 4066–4072. [CrossRef] [PubMed]
34. Bandoma, C.; Yeboah, P.; Gyan, K.; Rafiu, S.; Adusei, J.; Djan, G. Identification of potential cytochrome P450c 17 alpha inhibitors for the treatment of PCOS via scaffold hopping and fragment-based de-novo drug design. *J. Drug Des. Med. Chem.* **2024**, *10*, 31–44. [CrossRef]
35. Ghillace, A.; Chouitah, O.; Kiari, F.Z.; Fergoug, Z.; Daikh, Z. Phytochemical composition and antimicrobial activity of essential oil from the leaves of *Peganum harmala* L. in southern Algeria. *Acta Biol. Slov.* **2025**, *68*, 89–103. [CrossRef]
36. Anwar, F.; Ali, M.; Hussain, A.I.; Shahid, M. Antioxidant and antimicrobial activities of essential oil and extracts of fennel (*Foeniculum vulgare* Mill.) seeds from Pakistan. *Flavour Fragr. J.* **2009**, *24*, 170–176. [CrossRef]
37. Tahrouch, S.; Rapior, S.; Belahsen, Y.; Bessière, J.-M.; Andary, C. Volatile constituents of *Peganum harmala* (Zygophyllaceae). *Acta Bot. Gall.* **1998**, *145*, 121–124.
38. Nagpal, K.; Singh, S.K.; Mishra, D.N. Drug targeting to brain: A systematic approach to study the factors, parameters and approaches for prediction of permeability of drugs across BBB. *Expert Opin. Drug Deliv.* **2013**, *10*, 927–955. [CrossRef]
39. Arnott, J.A.; Planey, S.L. The influence of lipophilicity in drug discovery and design. *Expert Opin. Drug Discov.* **2012**, *7*, 863–875. [CrossRef]
40. Lipinski, C.A. Drug-like properties and the causes of poor solubility and poor permeability. *J. Pharmacol. Toxicol. Methods* **2000**, *44*, 235–249. [CrossRef]
41. Hou, T.; Wang, J.; Zhang, W.; Xu, X. ADME evaluation in drug discovery. 6. Can oral bioavailability in humans be effectively predicted by simple molecular property-based rules? *J. Chem. Inf. Model.* **2007**, *47*, 460–463. [CrossRef]
42. Stefanucci, A.; Iobbi, V.; Della Valle, A.; Scioli, G.; Pieretti, S.; Minosi, P.; Mirzaie, S.; Novellino, E.; Mollica, A. In silico identification of tripeptides as lead compounds for the design of KOR ligands. *Molecules* **2021**, *26*, 4767. [CrossRef]
43. Dalvie, D.; Nair, S.; Kang, P.; Loi, C.-M. Influence of aromatic rings on ADME properties of drugs. In *Metabolism, Pharmacokinetics and Toxicity of Functional Groups*; Royal Society of Chemistry: London, UK, 2010; pp. 275–327.
44. Zhang, Z.; Tang, W. Drug metabolism in drug discovery and development. *Acta Pharm. Sin. B* **2018**, *8*, 721–732. [CrossRef]
45. Muna, L.N. Identification of physicochemical properties, pharmacokinetics and toxicity of active compounds of *Kaempferia galanga* RHIZOME. *Med. Sains J. Ilm. Kefarmasian* **2024**, *9*, 317–324. [CrossRef]
46. Elmeliegy, M.; Vourvahis, M.; Guo, C.; Wang, D.D. Effect of P-glycoprotein (P-gp) inducers on exposure of P-gp substrates: Review of clinical drug–drug interaction studies. *Clin. Pharmacokinet.* **2020**, *59*, 699–714. [CrossRef] [PubMed]
47. Maurya, R.; Vikal, A.; Patel, P.; Narang, R.K.; Kurmi, B.D. Enhancing oral drug absorption: Overcoming physiological and pharmaceutical barriers for improved bioavailability. *AAPS PharmSciTech* **2024**, *25*, 228. [CrossRef] [PubMed]
48. Stamatovic, S.M.; Keep, R.F.; Andjelkovic, A.V. Brain endothelial cell-cell junctions: How to "open" the blood brain barrier. *Curr. Neuropharmacol.* **2008**, *6*, 179–192. [CrossRef]
49. Shubbar, Q.; Alchakee, A.; Issa, K.W.; Adi, A.J.; Shorbagi, A.I.; Saber-Ayad, M. From genes to drugs: CYP2C19 and pharmacogenetics in clinical practice. *Front. Pharmacol.* **2024**, *15*, 1326776. [CrossRef] [PubMed]

50. Daly, A.K.; Rettie, A.E.; Fowler, D.M.; Miners, J.O. Pharmacogenomics of CYP2C9: Functional and clinical considerations. *J. Pers. Med.* **2017**, *8*, 1. [CrossRef]
51. Nahid, N.A.; Johnson, J.A. CYP2D6 pharmacogenetics and phenoconversion in personalized medicine. *Expert Opin. Drug Metab. Toxicol.* **2022**, *18*, 769–785. [CrossRef]
52. Liu, Q.; Xie, Y.-j.; Qu, L.-h.; Zhang, M.-x.; Mo, Z.-c. Dyslipidemia involvement in the development of polycystic ovary syndrome. *Taiwan. J. Obstet. Gynecol.* **2019**, *58*, 447–453. [CrossRef]
53. Zhang, Y.; Wang, Z.; Wang, Y.; Jin, W.; Zhang, Z.; Jin, L.; Qian, J.; Zheng, L. CYP3A4 and CYP3A5: The crucial roles in clinical drug metabolism and the significant implications of genetic polymorphisms. *PeerJ* **2024**, *12*, e18636. [CrossRef]
54. Thorn, C.F.; Aklillu, E.; Klein, T.E.; Altman, R.B. PharmGKB summary: Very important pharmacogene information for CYP1A2. *Pharmacogenet. Genom.* **2012**, *22*, 73–77. [CrossRef]
55. Saganuwan, S. Toxicity studies of drugs and chemicals in animals: An overview. *Bulg. J. Vet. Med.* **2017**, *20*, 291–318. [CrossRef]
56. Amorim, A.M.; Piochi, L.F.; Gaspar, A.T.; Preto, A.J.; Rosario-Ferreira, N.; Moreira, I.S. Advancing drug safety in drug development: Bridging computational predictions for enhanced toxicity prediction. *Chem. Res. Toxicol.* **2024**, *37*, 827–849. [CrossRef]
57. Khan, M.Y.; Shah, A.U.; Duraisamy, N.; Cherkaoui, M.; Hemida, M.G. Repurposing of Some Nucleoside Analogs Targeting Some Key Proteins of the Avian H5N1 Clade 2.3.4.4 b to Combat the Circulating HPAI in Birds: An In Silico Approach. *Viruses* **2025**, *17*, 972. [CrossRef]
58. Tan, M.; Li, J.; Xu, H.E.; Melcher, K.; Yong, E.-L. Androgen receptor: Structure, role in prostate cancer and drug discovery. *Acta Pharmacol. Sin.* **2015**, *36*, 3–23. [CrossRef]
59. Joseph, R.; Binitha, R. Screening of potential antiandrogenic phytoconstituents and secondary metabolites of Terminalia chebula by docking studies. *Mater. Today Proc.* **2020**, *25*, 316–320. [CrossRef]
60. Suhandi, C.; Fadhilah, E.; Silvia, N.; Atusholihah, A.; Prayoga, R.R.; Megantara, S.; Muchtaridi, M. Molecular docking study of mangosteen (*Garcinia mangostana* L.) xanthone-derived isolates as anti androgen. *Indones. J. Cancer Chemoprev.* **2021**, *12*, 11–20. [CrossRef]
61. Death, A.K.; McGrath, K.C.; Handelsman, D.J. Valproate is an anti-androgen and anti-progestin. *Steroids* **2005**, *70*, 946–953. [CrossRef] [PubMed]
62. Kar, T.K.; Sil, S.; Ghosh, A.; Barman, A.; Chattopadhyay, S. Mitigation of letrozole induced polycystic ovarian syndrome associated inflammatory response and endocrinal dysfunction by *Vitex negundo* seeds. *J. Ovarian Res.* **2024**, *17*, 76. [CrossRef]
63. Usman, A.; Ahmad, M. Computational study suggesting reconsideration of BPA analogues based on their endocrine disrupting potential estimated by binding affinities to nuclear receptors. *Ecotoxicol. Environ. Saf.* **2019**, *171*, 154–161. [CrossRef]
64. Beg, M.A.; Beg, M.A.; Zargar, U.R.; Sheikh, I.A.; Bajouh, O.S.; Abuzenadah, A.M.; Rehan, M. Organotin antifouling compounds and sex-steroid nuclear receptor perturbation: Some structural insights. *Toxics* **2022**, *11*, 25. [CrossRef] [PubMed]
65. Dey, A.; Raza, M.T.; Limon, M.B.H. Virtual screening and identification of plant-based novel inhibitors of CYP17A1 in the treatment of polycystic ovarian syndrome (PCOS). *Next Res.* **2025**, *2*, 100452. [CrossRef]
66. Petrunak, E.M.; DeVore, N.M.; Porubsky, P.R.; Scott, E.E. Structures of human steroidogenic cytochrome P450 17A1 with substrates. *J. Biol. Chem.* **2014**, *289*, 32952–32964. [CrossRef]
67. Turcu, A.; Smith, J.M.; Auchus, R.; Rainey, W.E. Adrenal androgens and androgen precursors—Definition, synthesis, regulation and physiologic actions. *Compr. Physiol.* **2014**, *4*, 1369–1381. [CrossRef] [PubMed]
68. Mehralitabar, H.; Ghasemi, A.; Gholizadeh, J. Abiraterone and D4, 3-keto Abiraterone binding to CYP17A1, a structural comparison study by molecular dynamic simulation. *Steroids* **2021**, *167*, 108799. [CrossRef]
69. DeVore, N.M.; Scott, E.E. Structures of cytochrome P450 17A1 with prostate cancer drugs abiraterone and TOK-001. *Nature* **2012**, *482*, 116–119. [CrossRef]
70. Poulos, T.L.; Johnson, E.F. Structures of cytochrome P450 enzymes. In *Cytochrome P450: Structure, Mechanism, and Biochemistry*; Springer: Berlin/Heidelberg, Germany, 2015; pp. 3–32.
71. Wrobel, T.M.; Jørgensen, F.S.; Pandey, A.V.; Grudzinska, A.; Sharma, K.; Yakubu, J.; Bjorkling, F. Non-steroidal CYP17A1 inhibitors: Discovery and assessment. *J. Med. Chem.* **2023**, *66*, 6542–6566. [CrossRef]
72. Mahamed, R.R.; Maganhin, C.C.; Sasso, G.R.S.; de Jesus Simões, M.; Baracat, M.C.P.; Baracat, E.C.; Soares, J.M., Jr. Metformin improves ovarian follicle dynamics by reducing theca cell proliferation and CYP-17 expression in an androgenized rat model. *J. Ovarian Res.* **2018**, *11*, 18. [CrossRef]
73. Hirsch, A.; Hahn, D.; Kempná, P.; Hofer, G.; Nuoffer, J.-M.; Mullis, P.E.; Flück, C.E. Metformin inhibits human androgen production by regulating steroidogenic enzymes HSD3B2 and CYP17A1 and complex I activity of the respiratory chain. *Endocrinology* **2012**, *153*, 4354–4366. [CrossRef]
74. Bertrand, J.; Thieffine, S.; Vulpetti, A.; Cristiani, C.; Valsasina, B.; Knapp, S.; Kalisz, H.; Flocco, M. Structural characterization of the GSK-3β active site using selective and non-selective ATP-mimetic inhibitors. *J. Mol. Biol.* **2003**, *333*, 393–407. [CrossRef]
75. Kramer, T.; Schmidt, B.; Lo Monte, F. Small-Molecule Inhibitors of GSK-3: Structural Insights and Their Application to Alzheimer′ s Disease Models. *Int. J. Alzheimer's Dis.* **2012**, *2012*, 381029. [CrossRef] [PubMed]

76. Shen, W.; Lu, Y.-H. Molecular docking of citrus flavonoids with some targets related to diabetes. *Bangladesh J. Pharmacol.* **2013**, *8*, 156–170. [CrossRef]
77. Arfeen, M.; Patel, R.; Khan, T.; Bharatam, P.V. Molecular dynamics simulation studies of GSK-3β ATP competitive inhibitors: Understanding the factors contributing to selectivity. *J. Biomol. Struct. Dyn.* **2015**, *33*, 2578–2593. [CrossRef] [PubMed]

Disclaimer/Publisher's Note: The statements, opinions and data contained in all publications are solely those of the individual author(s) and contributor(s) and not of MDPI and/or the editor(s). MDPI and/or the editor(s) disclaim responsibility for any injury to people or property resulting from any ideas, methods, instructions or products referred to in the content.